Constitutive Modeling of Early-Age Concrete by a Stochastic Multi-scale Method

S. Liu[1], X. Liu[2,3], Y. Yuan[2] and H. A. Mang[4]

Abstract: A nonlinear viscoelastic constitutive model for early age concrete is presented in this paper. In this model, time-dependent properties, such as the elastic modulus, and thermal and autogenous shrinkage deformations, are computed by a stochastic multi-scale method, in which three different scales are specified according to the requirement of separation of scales, and different scales are linked by means of the asymptotic expansion theory with the help of specific representative volume elements (RVE). Thus, a cross-scale research from the cement paste to the macro structure of concrete is realized, and performance-based optimization of cement-based materials becomes possible. The developed constitutive model is implemented in commercial finite element software. Then, by means of a comparative study involving a numerical simulation and a full-scale experiment of a segment of the Hong Kong-Zhuhai-Macao immersed tunnel to obtain the temperature field and the strain field, the proposed constitutive model is validated. Thus a completely cross-scale constitutive model from the cement paste to the macro structure of concrete is realized, avoiding a variety of non-standardized and highly specialized test methods for concrete. After that, the stress field of the structure is analyzed. It is a prerequisite for structural analysis aimed at the investigation of cracking. Finally, taking different kinds of cement and aggregate as example, combinatorial optimization of material is conducted. And it is concluded that the type of cement and aggregate has an important influence on the early-age performance of investigated immersed tunnel. P.O.42.5 cement and limestone appears to be a good choice for control of cracking in engineering practice.

Keywords: Constitutive modeling, Early-age concrete, Stochastic multi-scale

[1] Department of Civil Engineering, Tongji University, Shanghai, China.

[2] State Key Laboratory for Hazard Reduction in Civil Engineering, Tongji University, Shanghai, China.

[3] Corresponding author. Email: Xian.liu@tongji.edu.cn (X. Liu)

[4] Institute of Mechanics of Materials and Structures, Vienna University of Technology, Vienna, Austria.

method, Thermal deformations, Autogenous shrinkage.

1   Instruction

In the construction of mass concrete structures, such as dams, immersed tunnels, basements, and wharfs, crack control at early-age has been an important aspect [Wang (1997)]. This is largely because of the volumetric deformation due to thermal [Bazant (1970)] and autogenous shrinkage deformations [Lura and Jensen (2003)]. At early age, the increase of the temperature due to the exothermic nature of hydration, followed by non-uniform cooling to ambient temperature, will lead to the formation of temperature gradients in concrete. These gradients and the resulting non-uniform thermal deformations within the element are responsible for the build-up of considerable thermal stresses [Ballim and Graham (2004); Amin and Kim (2009)]. On the other hand, most of the mixed water remains bound to the binder, which causes a reduction of the specific volume of water through chemical absorption during hydration. Therefore, small pores in the cement paste gradually develop. Accordingly, the vapor pressure and the relative humidity decreases. Closely related to this change of relative humidity, the cement paste undergoes autogenous shrinkage [Acker and Ulm (2001); Bentz (2008)]. This results in tensile stresses due to internal restraint from aggregates or external restraint from adjunct elements [Holt and Leivo (2006); Lura and Jensen (2009)]. Moreover, application of high strength concrete further increases the cracking risk because of the higher temperature rise and of larger volumetric deformations [Barcelo and Boivin (2001)].

Cracking of concrete reduces the load-carrying capacity of the structure; moreover, it may also lead to corrosion and rupture of the reinforcement. This reduces the durability of structures and finally causes structural damage [Ye and Tian (2013); Cao and Cheung (2013)]. Hence, it is necessary to establish a constitutive model applicable to early-age concrete, which takes into account the strong time-dependent mechanical properties and volumetric deformations. It can then be used to analyze the strain and stress field and provide technical support for cracking analysis of massive concrete structures at early age.

So far, different numerical approaches have been developed to investigate the early-age behavior of concrete structures. On the one hand, a temperature-stress coupling model has been established on the macro-scale, based on heat conduction theory and continuum mechanics, and related numerical analysis has been conducted to predict the temperature and stress development in concrete using the finite element method [Azenha and Faria (2009); Ilc and Turk (2009); Amin and Kim (2009); Briffaut and Benboud (2003)]. On the other hand, a numerical approach has been presented, which is based on multi-scale analysis and micro-mechanics. It is char-

acterized by linking the evolutionary material behavior with the ongoing hydration. For example, some researchers consider the hydration heat, autogenous shrinkage and strength growth by means of the chemo-mechanical, thermo-chemical and chemo-plastic couplings, and explore these cross-effects from the macro-scale of material modeling to the level of structural design [Ulm and Coussy (1995,1998); Hellmich (1999); Hellmich and Ulm (1999)]. Similar constitutive models have also been proposed to describe the interaction of hydration, shrinkage and the external load of concrete structures at early-age [Nguyen and Colina (2007); Nguyen and Nedjar (2007); Gawin and Pesavento (2006); Mohamad and Stéphane (2014)]. However, the accuracy or feasibility of these numerical models need further investigation when applied to cracking analysis of concrete structures at early-age, because the behavior of early-age concrete structures depends on both the time-dependent material properties and the structural restraints. Thus, more work is necessary to improve constitutive modeling of massive concrete structures at early age.

For research on volumetric deformations of concrete at early-age, the main focus is on the mechanism of thermal and autogenous shrinkage deformations [Paul and Allan (2007); Roman and Beat (2010); Jensen and Hansen (2001); Zhang and Hou (2010)] and on influence factors obtained from experiments on the macroscopic scale, considering the type of cement [Lura and Breugel (2001); Zhutovsky and Kovler (2004)], the aggregates [Idiart and Bisschop (2012)], the admixtures [Lee and Lee (2006); Yoo and Kwon (2012)], and external environmental factors [Jensen and Hansen (1999)]. Some researchers have developed models by fitting of data obtained from experiments, in form of linear functions, exponential functions, power functions or combinations of such functions [Chu and Kwon (2012)]. So far, there are two different ways to measure volumetric deformation of cement-based materials. One is the volumetric deformation method, whereas the other one is the one-dimensional deformation method [Yeon and Choi (2013); Maruyama and Teramoto (2011); Jensen and Hansen (1995); Bjøntegaard and Hammer (2004)]. For the cement paste and the mortar, the volumetric deformation method is standardized and well applied, because it can be measured at the beginning of the set, and easily operated with high precision. However, for concrete, there is no uniform standard test method. Different researchers have designed different experimental devices and methods, based on specific research goals and available laboratory conditions. In these tests, the concrete specimens should not only be sealed to prevent moisture exchange with the surrounding environment, but also measured without constraints of the deformations. The measurement should start already at the formation of the initial structure of concrete. Thus, it's highly specialized and expensive to accurately measure the volumetric deformation of concrete at early age.

The main reason of the problems mentioned above are that concrete, as a kind of multi-phase composite, consists of cement paste and aggregates; besides, along with the hydration reaction of cement, its early-age behavior shows a significant time variability. Multi-scale mechanics provides a new approach to treat problems of early-age concrete. Concrete is divided into different scales and it is assumed that it has a different composition and configuration at different scales, which are linked by means of homogenization strategies. This approach has been realized by micro-mechanics of composites, which has been used by several researchers [Bernard and Ulm (2003); Pichler and Lackner (2007); Zhang and Hou (2012); Ghabezloo (2011)]. However, in these models some assumptions have been made to simplify the calculations, which do not reflect the random configuration of concrete. Since concrete is a typical non-homogeneous composite, its mechanical properties and volumetric deformations depend not only on the hydration of the cement paste, but also on the properties of the constituents and of their distribution. In order to take these characteristics into account, multi-inclusion unit cell models which allow a direct numerical simulations of complex heterogeneous materials and structures have been proposed [Dong and Atluri (2012, 2013)]. Asymptotic expansion theory has been proposed as a calculation method [Kesavan (1979)]. It is suitable for composite materials with a periodic or a random configuration with high inclusion content, and it accounts well for the interaction between inclusions [Cui and Shin (1999); Bohm and Han (2004); Du and Jiang (2011)]. Moreover, it has been successfully applied to the computation of mechanical and thermal properties of materials with random distribution of multi-scale grains [Li and Cui (2005); Feng and Cui (2004)].

Thus, the main objective of this research is to establish a nonlinear viscoelastic constitutive model for early age concrete. In this model, time-dependent properties are computed by a stochastic multi-scale method. Another objective is the implementation of this constitutive model in finite element software and validation of its effectiveness by means of a full scale experiment of the Hong Kong-Zhuhai-Macao (HZM) immersed tunnel. Then, the stress field is computed, which provides the basis for the analysis of structural cracking. Finally, the influence of the type of cement and of the aggregates is investigated.

2   Fundamentals of the asymptotic expansion theory

A point of a homogeneous body can be treated as a periodic multiple permutation of the RVE, which is heterogeneous in the asymptotic expansion theory [Cui and Shin (1999)], as shown in Fig. 1.

In Fig. 2.1, Γ_u and Γ_t denote the displacement and the stress boundary; $\varepsilon(0 < \varepsilon << 1)$ represents the ratio of magnification between the two scales; $\mathbf{x}$ denotes the
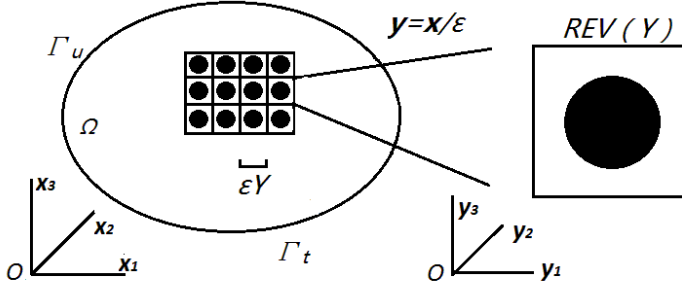
Figure 1: Periodic composite with a small period.

global coordinate; **y** denotes the local coordinate. As ε tends to zero, the composite material becomes a homogeneous elastomer.

When the equivalent homogeneous body is subjected to external forces, its field quantities, such as the displacements, the strains, and the stresses, vary with the global coordinate **x**. Because of the high heterogeneity of the local constitution, they also vary rapidly with the local coordinate **y**. The governing equation of the mechanical behavior of deformable solids is given as [Cui and Shin (1999)]:

$$\frac{\partial}{\partial x_j}\left[C_{ijkl}^{\varepsilon}(\pmb{x})\left(\frac{1}{2}\left(\frac{\partial u_k^{\varepsilon}(\pmb{x})}{\partial x_l}+\frac{\partial u_l^{\varepsilon}(\pmb{x})}{\partial x_k}\right)\right)\right]=f_i(\pmb{x}), \quad \pmb{x}\in\Omega \tag{1}$$

In Eq. (1), $C_{ijkl}^{\varepsilon}(\pmb{x})$ denotes a component of the elastic tensor, $u_k^{\varepsilon}(\pmb{x})$ and $u_l^{\varepsilon}(\pmb{x})$ represent two components of displacement vector at point **x** of the equivalent homogeneous body, and $f_i(\pmb{x})$ is a component of the vector of volume force. The boundary conditions are specified as follows [Cui and Shin (1999)]:

$$u_i^{\varepsilon}(\pmb{x})=\bar{u}_i(\pmb{x}), \quad \pmb{x}\in\Gamma_u \tag{2}$$

$$v_j C_{ijkl}^{\varepsilon}(\pmb{x})\frac{1}{2}\left(\frac{\partial u_k^{\varepsilon}(\pmb{x})}{\partial x_l}+\frac{\partial u_l^{\varepsilon}(\pmb{x})}{\partial x_k}\right)=\bar{p}_i(\pmb{x}), \quad \pmb{x}\in\Gamma_t \tag{3}$$

where, $\bar{u}_i(\pmb{x})$ denotes a component of the displacement vector on displacement boundary Γ_u, $\bar{p}_i(\pmb{x})$ denotes a component of the stress vector on stress boundary, v_j denotes a component of the unit normal vector on Γ_p.

The properties of the material composition in the RVE can be expressed as:

$$C_{ijkl}^{\varepsilon}(\pmb{x})=C_{ijkl}(\pmb{y}) \tag{4}$$

Considering not only the homogeneous behavior but also the local configuration of the material, an asymptotic expansion of $\boldsymbol{u}^\varepsilon(\boldsymbol{x})$ is performed with the help of the coordinates $\boldsymbol{x} = (x_1, x_2, x_3)$ and $\boldsymbol{y} = (y_1, y_2, y_3)$:

$$\boldsymbol{u}^\varepsilon(\boldsymbol{x}) = \boldsymbol{u}^0(\boldsymbol{x}) + \sum_{l=1}^\infty \varepsilon^l \sum_{a_1\ldots a_l = 1\ldots n} \mathrm{N}_{a_1\ldots a_l}(\boldsymbol{y}) \frac{\partial^l \boldsymbol{u}^0(\boldsymbol{x})}{\partial x_{a_1} \partial x_{a_2}\ldots \partial x_{a_l}} \tag{5}$$

$$\mathrm{N}_{a_1\ldots a_l}(\boldsymbol{y}) = \begin{pmatrix} N_{a_1\ldots a_l}^{11}(\boldsymbol{y}) & \cdots & N_{a_1\ldots a_l}^{1n}(\boldsymbol{y}) \\ \vdots & \cdots & \vdots \\ N_{a_1\ldots a_l}^{n1}(\boldsymbol{y}) & \cdots & N_{a_1\ldots a_l}^{nn}(\boldsymbol{y}) \end{pmatrix} \tag{6}$$

In Eq. (5), $\boldsymbol{u}^0(\boldsymbol{x})$ is the homogenized displacement, $\boldsymbol{N}_{a_1\ldots a_l}(\boldsymbol{y})$ is a matrix function, which reflects the influence of the local heterogeneity of the composites.

Differentiation with respect to **x** is defined as:

$$\frac{\partial}{\partial x_i} = \frac{\partial}{\partial x_i} + \varepsilon^{-1} \frac{\partial}{\partial y_i} \tag{7}$$

Substituting Eq. (5) into Eq. (1) and letting $\varepsilon \to 0$, the coefficients of the terms $\varepsilon^n (n = -2, -1, 0)$ must be zero. Consequently, a series of partial differential equations is obtained. Then, the matrix function $\boldsymbol{N}_{a_1\ldots a_l}(\boldsymbol{y})$ can be determined by solving these differential equations in the RVE. The coefficient $C_{ijst}^H(\boldsymbol{x})$ of the homogenized elastic tensor is obtained as:

$$C_{ijst}^H(\boldsymbol{x}) = \frac{1}{|Y|} \int_Y C_{ijkl}(\boldsymbol{y}) \left(\delta_{ks}\delta_{lt} + \frac{\partial N_k^{st}}{\partial y_l} \right) dz \tag{8}$$

The homogenized displacement $\boldsymbol{u}^0(\boldsymbol{x})$ can then be determined from:

$$\frac{\partial}{\partial x_j} \left[C_{ijkl}^H(\boldsymbol{x}) \left(\frac{\partial u_k^0(\boldsymbol{x})}{\partial x_l} + \frac{\partial u_l^0(\boldsymbol{x})}{\partial x_k} \right) \right] = f_i(\boldsymbol{x}) \tag{9}$$

The displacement field $\boldsymbol{u}^\varepsilon(\boldsymbol{x})$, which considers the effect of the local constitution can be obtained. Based on the geometric and physical equations of the theory of elasticity, more accurate stress and strain fields can be obtained [Cui and Shin (1999)].

3   Constitutive modeling of early-age concrete by multi-scale method

Determination of the stress and strain field by means of the theory of elasticity involves three equilibrium equations, six constitutive equations and six geometric equations. The incremental form of these equations reads as:

$$\Delta\sigma_{ji,j} + \Delta p_i = 0 \tag{10}$$

$$\Delta\sigma_{ij} = C_{ijkl}\Delta\varepsilon_{ij} \tag{11}$$

$$\Delta\varepsilon_{ij} = \frac{1}{2}(\Delta u_{i,j} + \Delta u_{j,i}) \tag{12}$$

At its early age, the concrete is in a state of tensile stresses and low compressive stresses. Besides, due to the characteristics of concrete at early age, the structural deformations can be divided into: (1) time-independent elastic deformations, and (2) time-dependent viscoelastic deformations, such as thermal and autogenous shrinkage deformations. Therefore, the nonlinear viscoelastic constitutive model for early age concrete is established, where the time-dependent properties are described in an incremental form. The total strain increment is composed of three different parts:

$$\Delta\boldsymbol{\varepsilon}(t_n) = \Delta\boldsymbol{\varepsilon}^e(t_n) + \Delta\boldsymbol{\varepsilon}^{th}(t_n) + \Delta\boldsymbol{\varepsilon}^{sh}(t_n) \tag{13}$$

In Eq. (13), $\Delta\boldsymbol{\varepsilon}$ is an increment of the total strain, $\Delta\boldsymbol{\varepsilon}^e$ is an increment of the elastic strain caused by loads, $\Delta\boldsymbol{\varepsilon}^{th}$ is an increment of the thermal strain resulting from temperature variation due to hydration, and $\Delta\boldsymbol{\varepsilon}^{sh}$ is an increment of the shrinkage strain resulting from autogenous shrinkage. Thus, an increment of the elastic strain can be expressed as:

$$\Delta\boldsymbol{\varepsilon}^e(t_n) = \Delta\boldsymbol{\varepsilon}(t_n) - \Delta\boldsymbol{\varepsilon}^{th}(t_n) - \Delta\boldsymbol{\varepsilon}^{sh}(t_n) \tag{14}$$

Substituting Eq. (14) into Eq. (11), gives:

$$\Delta\sigma_{ij}(t_n) = C^e_{ijkl}(t_n)\Delta\varepsilon^e_{kl}(t_n) = C^e_{ijkl}(t_n)(\Delta\varepsilon_{kl}(t_n) - \Delta\varepsilon^{th}_{kl}(t_n) - \Delta\varepsilon^{sh}_{kl}(t_n)) \tag{15}$$

Thermal strain can be obtained:

$$\Delta\boldsymbol{\varepsilon}^{th}(t_n) = \boldsymbol{a}(t_n)\Delta T(t_n) \tag{16}$$

where, $\boldsymbol{a}(t_n)$ is the tensor of time-dependent thermal expansion coefficients (CTE); $\Delta T(t_n)$ is the temperature increment. In the constitutive model, time-dependent properties, such as the elasticity tensor $\boldsymbol{C}^e(t_n)$, the tensor of thermal expansion coefficients $\boldsymbol{a}(t_n)$, and the autogenous shrinkage strains, $\boldsymbol{\varepsilon}^{sh}(t_n)$, are computed by a stochastic multi-scale method.

3.1 Representation

Below the macro-scale, three different scales will be considered: the concrete scale, the mortar scale, and the cement paste scale. This is in accordance with the requirement of separation of scales [Liu and Liu (2013,2014)], as shown in Fig. 2.
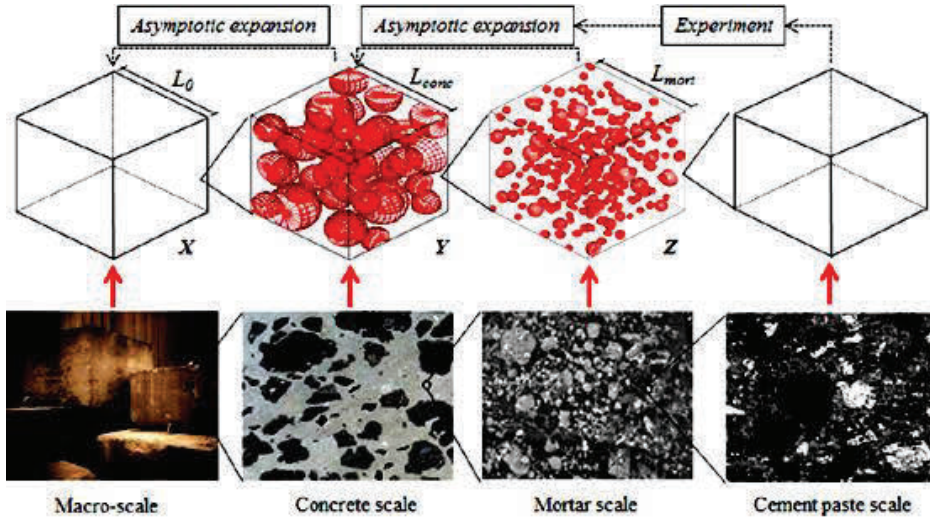
Figure 2: Scales division.

The cement paste is regarded as isotropic and homogeneous. Its mechanical parameters and the volumetric deformations are obtained from standardized and highly precise tests.

The mortar is considered as a two-phase composite which consists of the cement paste as the matrix and sand as the inclusion. Therefore, a series of specific RVE are proposed. Each of them is assumed to consist of the matrix and of spherical inclusions which are non-overlapping and distributed randomly, as shown in Fig. 2. A spherical inclusion is defined by four parameters: the position of its center (y_1^n, y_2^n, y_3^n), and the diameter D_{sand}. With regard to these specific RVEs for mortar, their length L_{mort} is equal to $1cm$, and the diameter of the spheres, D_{sand}, is equal to $0.25 - 1.0mm$. It is remarkable that (y_1^n, y_2^n, y_3^n) and D_{sand} are subject to uniform distributions within their own range.

At the concrete scale, the homogenized mortar represents the matrix and the coarse aggregates are the inclusions. Hence, at this scale material is also treated as a two-phase composite too. A series of specific RVEs which simulate the random distribution of coarse aggregates in the mortar is described the in same way as for the mortar scale, as is also shown in Fig 3.1. With regard to these specific RVEs for the concrete scale, the size of them, L_{conc}, is $20cm$, the diameter of spheres is $5 - 20mm$.

Because of $D_{sand} << L_{mort} \leq D_{aggr} << L_{conc} << L_0$, where L_0 characterizes the macro-scale, the requirement of separation of scales is satisfied.

3.2 Multi-scale analysis of the elastic modulus

According to the multi-scale representation above, the scale factor ε_{conc} at the concrete scale is defined as $\varepsilon_{conc} = \varepsilon$, where ε denotes the basic scale factor. At the mortar scale, the scale factor ε_{mort} is obtained as $\varepsilon_{mort} = \varepsilon^2$. For the sake of simplicity, the probability distributions w^{conc} and w^{mort} are denoted as w, given as $w = \{w^{conc} : \mathbf{y} \in Y; w^{mort} : z \in Z\}$, as shown in Fig 3.
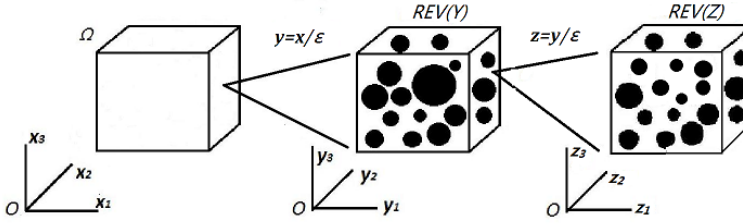
Figure 3: Representation of multi-scale method.

With the help of the elasticity tensor, the properties of the material composition in the RVE can be expressed as follows:

$$C^{\varepsilon}_{ijkl}(\mathbf{x}) = C_{ijkl}(\mathbf{y}, w^1) = C_{ijkl}(\mathbf{y}, \mathbf{z}, w^2) \tag{17}$$

Let **x, y, z** denote the coordinate systems of the macro scale, the concrete scale, and the mortar scale, respectively. They are related to one another as follows:

$$\mathbf{y} = \mathbf{x}/\varepsilon, \quad \mathbf{z} = \mathbf{y}/\varepsilon \tag{18}$$

An asymptotic expansion of $\mathbf{u}^{\varepsilon}(\mathbf{x})$ is formed with coordinates x, y and z:

$$\mathbf{u}^{\varepsilon}(\mathbf{x}) = \mathbf{u}^0(\mathbf{x}) + \varepsilon \mathbf{u}^1(\mathbf{x}, \mathbf{y}) + \varepsilon^2 \mathbf{u}^2(\mathbf{x}, \mathbf{y}, \mathbf{z}) + ... \tag{19}$$

Differentiation with respect to **x** is defined as:

$$\frac{\partial}{\partial x_i} = \frac{\partial}{\partial x_i} + \varepsilon^{-1}\frac{\partial}{\partial y_i} + \varepsilon^{-2}\frac{\partial}{\partial z_i} \tag{20}$$

Substituting Eq. (19) into Eq. (1) and letting $\varepsilon \to 0$, the coefficients of each term $\varepsilon^n (n = -4, -3, -2, -1)$ must be zero. The following partial differential equation is the vanishing coefficient of ε^{-4}:

$$\frac{\partial}{\partial z_j}\left(C_{ijkl}(\mathbf{y}, \mathbf{z}, w)\frac{\partial u_k^0}{\partial z_l}\right) = 0 \tag{21}$$

Since $\boldsymbol{u}^0$ is only a function of $\mathbf{x}$, the above relation is automatically satisfied. The following partial differential equation represents the vanishing coefficient of ε^{-3}:

$$\frac{\partial}{\partial y_j}\left(C_{ijkl}(\boldsymbol{y},\boldsymbol{z},w)\frac{\partial u_k^0}{\partial z_l}\right) + \frac{\partial}{\partial z_j}\left(C_{ijkl}(\boldsymbol{y},\boldsymbol{z},w)\left(\frac{\partial u_k^0}{\partial y_l}+\frac{\partial u_k^1}{\partial z_l}\right)\right) = 0 \tag{22}$$

Since $\boldsymbol{u}^0$ is only a function of $\mathbf{x}$, the terms $\partial u_k^0/\partial z_l$ and $\partial u_k^0/\partial y_l$ vanish. Thus, $\boldsymbol{u}^1$ is a function of $\mathbf{x}$ and $\mathbf{y}$, which can be written as follows:

$$u_i^1(\boldsymbol{x},\boldsymbol{y}) = N_i^{kl}(\boldsymbol{y})\frac{\partial u_k^0}{\partial x_l} \tag{23}$$

$\boldsymbol{N}(\boldsymbol{y})$ is a matrix function defined in the RVE(Y) at the concrete scale, which reflects the influence of the local heterogeneity of the composites. Recalling that $\boldsymbol{u}^0$ is only a function of $\mathbf{x}$, and $\boldsymbol{u}^1$ is a function of $\mathbf{x}$ and $\mathbf{y}$, the partial differential equation represents the vanishing coefficient of ε^{-2} can be simplified as follows:

$$\frac{\partial}{\partial z_j}\left[C_{ijkl}(\boldsymbol{y},\boldsymbol{z},w)\left(\frac{\partial u_k^0}{\partial x_l}+\frac{\partial u_k^1}{\partial y_l}+\frac{\partial u_k^2}{\partial z_l}\right)\right] = 0 \tag{24}$$

The term $\partial u_k^0/\partial x_l$ is a function of $\mathbf{x}$ and the term $\partial u_k^1/\partial y_l$ is a function of $\mathbf{x}$ and $\mathbf{y}$. This allows writing $\boldsymbol{u}^2$ as follows:

$$u_i^2(\boldsymbol{x},\boldsymbol{y},\boldsymbol{z}) = M_i^{kl}(\boldsymbol{z})\left(\delta_{km}\delta_{ln}+\frac{\partial N_k^{mn}}{\partial y_l}\right)\frac{\partial u_m^0}{\partial x_n} \tag{25}$$

$\boldsymbol{M}(\boldsymbol{z})$ is matrix function defined in the RVE (Z) at the mortar scale, it reflects the influence of the local configuration of the composites. Substituting Eq. (23) and Eq. (25) into Eq. (24), gives:

$$
\begin{aligned}
&C_{ijkl}(\boldsymbol{y},\boldsymbol{z},w)\left(\frac{\partial u_k^0}{\partial x_l}+\frac{\partial u_k^1}{\partial y_l}+\frac{\partial u_k^2}{\partial z_l}\right)\\
&= C_{ijkl}(\boldsymbol{y},\boldsymbol{z},w)\left(\delta_{ks}\delta_{lt}+\frac{\partial M_k^{st}}{\partial z_l}\right)\left(\delta_{ms}\delta_{nt}+\frac{\partial N_s^{mn}}{\partial y_t}\right)\frac{\partial u_m^0}{\partial x_n}
\end{aligned}
\tag{26}
$$

Substituting Eq. (26) into Eq. (24) yields the partial differential equations for the mortar scale equation in RVE Z, which is the equation for determination of$\mathbf{M}(\mathbf{z})$:

$$\frac{\partial}{\partial z_j}\left[C_{ijkl}(\boldsymbol{y},\boldsymbol{z},w)\left(\delta_{ks}\delta_{lt}+\frac{\partial M_k^{st}}{\partial z_l}\right)\right] = 0 \tag{27}$$

It is seen that $M(z)$ depends only on the coordinate z for the mortar scale. The following simplified partial differential equation represents the vanishing coefficient of ε^{-1}:

$$\frac{\partial}{\partial y_j}\left[C_{ijkl}(y,z,w)\left(\frac{\partial u_k^0}{\partial x_l}+\frac{\partial u_k^1}{\partial y_l}+\frac{\partial u_k^2}{\partial z_l}\right)\right]+\frac{\partial}{\partial z_j}\left[C_{ijkl}(y,z,w)\left(\frac{\partial u_k^1}{\partial x_l}+\frac{\partial u_k^2}{\partial y_l}+\frac{\partial u_k^3}{\partial z_l}\right)\right]=0$$

(28)

The volume average of quantities for the mortar scale domain Z is defined as

$$\langle\bullet\rangle_2 = \frac{1}{|Z|}\int_Z \bullet dz$$

(29)

Substitution of Eq. (26) into Eq. (28) with the help of Eq. (3.120) yields the following equation for determination of $N(y)$ in RVE (Y) at the concrete scale:

$$\frac{\partial}{\partial y_j}\left[C_{ijst}^{H_1}(y,w)\left(\delta_{ms}\delta_{nt}+\frac{\partial N_s^{mn}}{\partial y_t}\right)\right]=0$$

(30)

In Eq. (30), $C_{ijst}^{H_1}(y,w)$ is a coefficient of the elasticity tensor of the homogenized mortar, given as follows:

$$C_{ijst}^{H_1}(y,w) = \frac{1}{|Z|}\int_Z C_{ijkl}(y,z,w)\left(\delta_{ks}\delta_{lt}+\frac{\partial M_k^{st}}{\partial z_l}\right)dz$$

(31)

Thus, $N(y)$ is obtained from Eq. (30), making use of Eq. (31). The following partial differential equation represents the vanishing coefficient of ε^0:

$$\frac{\partial}{\partial x_j}\left[C_{ijkl}(y,z,w)\left(\frac{\partial u_k^0}{\partial x_l}+\frac{\partial u_k^1}{\partial y_l}+\frac{\partial u_k^2}{\partial z_l}\right)\right]+\frac{\partial}{\partial y_j}\left[C_{ijkl}(y,z,w)\left(\frac{\partial u_k^1}{\partial x_l}+\frac{\partial u_k^2}{\partial y_l}+\frac{\partial u_k^3}{\partial z_l}\right)\right]$$
$$+\frac{\partial}{\partial z_j}\left(C_{ijkl}(y,z,w)\left(\frac{\partial u_k^2}{\partial x_l}+\frac{\partial u_k^3}{\partial y_l}+\frac{\partial u_k^4}{\partial z_l}\right)\right)=f_i$$

(32)

The volume average of quantities for the mortar scale domain Y is defined as:

$$\langle\bullet\rangle_1 = \frac{1}{|Y|}\int_Y \bullet dy$$

(33)

Substitution of Eq. (26) into Eq. (32) with the help of Eq. (29) and Eq. (33) yields the following equation for the concrete scale is obtained:

$$\frac{\partial}{\partial x_j}\left[C_{ijkl}^{H}(w)\left(\frac{\partial u_k^0}{\partial x_l}\right)\right]=f_i$$

(34)

In Eq. (34), $C_{ijkl}^{H}(w)$ is a coefficient of the elasticity tensor of the homogenized concrete scale, denoted as:

$$C_{ijkl}^{H}(w) = \frac{1}{|Y|} \int_{Y} C_{ijst}^{H_1}(\mathbf{y}, w) \left(\delta_{ks} \delta_{lt} + \frac{\partial N_s^{kl}}{\partial y_t} \right) dy \qquad (35)$$

3.3 *Multi-scale analysis of the CTE [Liu and Liu (2013)]*

Multi-scale analysis of the CTE is similar to the multi-scale analysis of the elastic modulus. The scales and the proposed multi-scale method are the same as shown in Fig. 2 and Fig. 3 However, thermal expansion, in general, represents a form of a coupled thermal-mechanical problem; CTE connects the thermal and mechanical behavior. The governing equation can be described as follows:

$$\frac{\partial}{\partial x_j} \left[C_{ijkl}^{\varepsilon}(\mathbf{x}) \left(\frac{1}{2} \left(\frac{\partial u_k^{\varepsilon}(\mathbf{x})}{\partial x_l} + \frac{\partial u_l^{\varepsilon}(\mathbf{x})}{\partial x_k} \right) - a_{kl}^{\varepsilon}(\mathbf{x}) T(\mathbf{x}) \right) \right] = f_i(\mathbf{x}), \ \mathbf{x} \in \Omega \qquad (36)$$

In Eq. (36), $a_{kl}^{\varepsilon}(\mathbf{x})$ are components of the tensor of the thermal expansion coefficients, $\theta^0(\mathbf{x})$ is the homogeneous temperature field. The boundary conditions are specified as follows:

$$T^{\varepsilon}(\mathbf{x}) = \bar{T}(\mathbf{x}), \ \mathbf{x} \in \Gamma_1, \quad u_i^{\varepsilon}(\mathbf{x}) = \bar{u}_i(\mathbf{x}), \ \mathbf{x} \in \Gamma_2 \qquad (37)$$

In Eq. (37), Γ_1 denotes the temperature boundary and Γ_2 stands for the displacement boundary, $\bar{\theta}(\mathbf{x})$ and $\bar{\mathbf{u}}(\mathbf{x})$ denote the corresponding boundary values.

Considering not only the homogeneous mechanical behavior but also the local configuration of the material, Eq. (19) is substituted into Eq. (36), followed by letting $\varepsilon \to 0$. The coefficients of the terms $\varepsilon^n (n = -4, -3, -2, -1)$ must be zero. Then, similar as in section 3.2, the matrix function $\mathbf{M}(\mathbf{z})$ defined in the RVE (Z) at the mortar scale and the matrix function $\mathbf{N}(\mathbf{y})$ defined in the RVE (Y) at the concrete scale, are obtained from Eq. (27) and Eq. (30). The stiffness coefficients of the homogenized mortar scale, $C_{ilst}^{H_1}(\mathbf{y}, w)$, and of the homogenized the concrete scale, $C_{ijkl}^{H}(w)$, are computed according to Eq. (31) and Eq. (35), respectively.

Then, comes different partial differential equation represents the vanishing coefficient of ε^0

$$\frac{\partial}{\partial x_j} \left[C_{ijkl}(\mathbf{y}, \mathbf{z}, w) \left(\frac{\partial u_k^0}{\partial x_l} + \frac{\partial u_k^1}{\partial y_l} + \frac{\partial u_k^2}{\partial z_l} \right) \right] + \frac{\partial}{\partial y_j} \left[C_{ijkl}(\mathbf{y}, \mathbf{z}, w) \left(\frac{\partial u_k^1}{\partial x_l} + \frac{\partial u_k^2}{\partial y_l} \right) \right]$$

$$+ \frac{\partial}{\partial z_j} \left(C_{ijkl}(\mathbf{y}, \mathbf{z}, w) \frac{\partial u_k^2}{\partial x_l} \right) - \frac{\partial}{\partial x_j} \left(C_{ijkl}(\mathbf{y}, \mathbf{z}, w) a_{kl}(\mathbf{y}, \mathbf{z}, w) T(x) \right) = f_i$$

$$(38)$$

Substitution of Eq. (26) into Eq. (38) with the help of Eq. (29) and Eq. (33) yields the following equation for the concrete scale:

$$\frac{\partial}{\partial x_j} \left[C_{ijkl}^H(w) \frac{\partial u_k^0}{\partial x_l} - \Theta T(x) \right] = f_i \tag{39}$$

In Eq. (39), Θ is defined as:

$$\Theta = \int_Y \int_Z C_{ijkl}(\boldsymbol{y}, \boldsymbol{z}, w) a_{kl}(\boldsymbol{y}, \boldsymbol{z}, w) dz dy \tag{40}$$

According to Eq. (36) and Eq. (39), Θ can also be written as:

$$\Theta = C_{ijkl}^H(w) a_{kl}^H(w) \tag{41}$$

Finally, the homogenized CTE at the macro-scale is obtained as:

$$a_{kl}^H(w) = \Theta \left[C_{ijkl}^H(w) \right]^{-1} \tag{42}$$

3.4 Multi-scale analysis of the autogenous shrinkage strains [Liu and Liu (2014)]

Multi-scale analysis of the autogenous shrinkage strains is similar to the multi-scale analysis of the elastic modulus too. The scales and the proposed multi-scale method are the same as shown in Fig. 2 and Fig. 3. However, autogenous shrinkage represents the bulk deformation of a closed, isothermal, cement-based material system which is not subjected to external forces. Therefore, the body forces and the boundary conditions are equal to zero, which is different from Eq. (1) to Eq. (3). Modified equation of autogenous shrinkage can be expressed as:

$$\frac{\partial}{\partial x_j} \left[C_{ijkl}^\varepsilon(\boldsymbol{x}) \left(\frac{1}{2} \left(\frac{\partial u_k^\varepsilon(\boldsymbol{x})}{\partial x_l} + \frac{\partial u_l^\varepsilon(\boldsymbol{x})}{\partial x_k} \right) - \varepsilon_{kl}^\varepsilon(\boldsymbol{x}) \right) \right] = 0, \quad \boldsymbol{x} \in \Omega \tag{43}$$

In Eq. (43), $\varepsilon_{kl}^\varepsilon(\boldsymbol{x})$ denotes a component of the strain tensor due to autogenous shrinkage at point **x** of equivalent homogeneous body. Then, analogous to section 3.2, the matrix function $\boldsymbol{M}(\boldsymbol{z})$, defined in the RVE (Z) and the matrix function $\boldsymbol{N}(\boldsymbol{y})$, defined in the RVE (Y), and the coefficient of the elasticity tensor at the mortar scale $C_{ilst}^{H_1}(\mathbf{y}, w)$, as well as the coefficient $C_{ijkl}^H(w)$ at the concrete scale.

The partial differential equation that represents the vanishing coefficient of ε^0 is obtained as:

$$\frac{\partial}{\partial x_j}\left[C_{ijkl}(\mathbf{y},\mathbf{z},w)\left(\frac{\partial u_k^0}{\partial x_l}+\frac{\partial u_k^1}{\partial y_l}+\frac{\partial u_k^2}{\partial z_l}\right)\right]+\frac{\partial}{\partial y_j}\left[C_{ijkl}(\mathbf{y},\mathbf{z},w)\left(\frac{\partial u_k^1}{\partial x_l}+\frac{\partial u_k^2}{\partial y_l}+\frac{\partial u_k^3}{\partial z_l}\right)\right]$$

$$+\frac{\partial}{\partial z_j}\left(C_{ijkl}(\mathbf{y},\mathbf{z},w)\left(\frac{\partial u_k^2}{\partial x_l}+\frac{\partial u_k^3}{\partial y_l}+\frac{\partial u_k^4}{\partial z_l}\right)\right)-\frac{\partial}{\partial x_j}\left(C_{ijkl}(\mathbf{y},\mathbf{z},w)\varepsilon_{kl}^0(\mathbf{x})\right)=0$$

$$(44)$$

Substitution of Eq. (26) into Eq. (44) with the help of Eq. (29) and Eq. (33) yields the following equation for the concrete scale:

$$\frac{\partial}{\partial x_j}\left[C_{ijkl}^H(w)\left(\frac{\partial u_k^0}{\partial x_l}-\varepsilon_{kl}^0\right)\right]=0 \tag{45}$$

Letting $\varepsilon \to 0$, the strain field in the mortar scale domain Z is obtained as:

$$\varepsilon_{kl}^2=\frac{1}{2}\left(\frac{\partial u_k^0}{\partial x_l}+\frac{\partial u_l^0}{\partial x_k}+\frac{\partial u_k^1}{\partial y_l}+\frac{\partial u_l^1}{\partial y_k}+\frac{\partial u_k^2}{\partial z_l}+\frac{\partial u_l^2}{\partial z_k}\right) \tag{46}$$

Substitution of Eq. (23) and Eq. (25) into Eq. (46) gives:

$$\begin{aligned}\varepsilon_{kl}^2=&\frac{1}{2}\left(\frac{\partial u_k^0}{\partial x_l}+\frac{\partial u_l^0}{\partial x_k}\right)\\&+\frac{1}{2}\frac{\partial u_m^0}{\partial x_n}\left[\left(\delta_{pm}\delta_{qn}+\frac{\partial N_p^{mn}}{\partial y_q}\right)\left(\frac{\partial M_k^{pq}}{\partial z_l}+\frac{\partial M_l^{pq}}{\partial z_k}\right)+\left(\frac{\partial N_k^{mn}}{\partial y_l}+\frac{\partial N_l^{mn}}{\partial y_k}\right)\right]\end{aligned} \tag{47}$$

In Eq. (47), the strains of the matrix in the domain Z are the strains of the cement paste ε_{c-p}. They can be obtained from tests, which can be performed easily, providing high-precision data. Thus, the homogenized displacement field $\mathbf{u}^0$ can be computed, followed by determination of $\mathbf{u}^1$ and $\mathbf{u}^2$. The strain field in the concrete scale domain Y is given as:

$$\varepsilon_{kl}^1=\frac{1}{2}\left(\frac{\partial u_k^0}{\partial x_l}+\frac{\partial u_l^0}{\partial x_k}+\frac{\partial u_k^1}{\partial y_l}+\frac{\partial u_l^1}{\partial y_k}\right) \tag{48}$$

Substitution of $\mathbf{u}^0$, $\mathbf{u}^1$ and $\mathbf{N}(\mathbf{y})$ into Eq. (48) gives:

$$\varepsilon_{kl}^1=\frac{1}{2}\left(\frac{\partial u_k^0}{\partial x_l}+\frac{\partial u_l^0}{\partial x_k}\right)+\frac{1}{2}\frac{\partial u_m^0}{\partial x_n}\left(\frac{\partial N_k^{mn}}{\partial y_l}+\frac{\partial N_l^{mn}}{\partial y_k}\right) \tag{49}$$

In Eq. (49), the strains of the matrix in the domain Y are the strains of the equivalent homogenized mortar ε_{mort}. Substitution of $\mathbf{u}^0$ into Eq. (45) gives the homogenized strains $\boldsymbol{\varepsilon}^0$ of the macro scale, caused by autogenous shrinkage, can be obtained.

3.5   Analysis procedure

ABAQUS is a powerful finite element software. One of its advantages is that it provides the subroutine interface, allowing users to implement constitutive models through C or FORTRAN programs. The program of the constitutive model for early-age concrete, proposed in this research, consists of two subroutines: the subroutine HEAT, developed to simulate the generation of hydration heat, and the subroutine UEXPAN, dealing with the relations between stress and different kinds of strain. Thus, on the assumption that the thermal problem is independent of the mechanical problem, the application of this constitutive model is divided into two stages.

1. Simulation of the temperature field

At first, the density, the specific heat, and the heat transfer coefficient are inputted into the computer program. The temperature field is simulated by means of the calculation of the heat flow in ABAQUS/Standard. Then, the generation of the hydration heat is simulated with the help of the subroutine HEAT. The output at this stage is the temperature at the nodes of the finite element mesh It is stored in the ODB file along with the time step.

2. Simulation of the stress field

Next, the stain field is simulated. This is a typical thermal-mechanical coupled problem. It is determined by the calculation of the thermal strains, based on the thermal analysis described previous, together with the autogenous shrinkage strains. Thus, the stress field is obtained. In these calculations, the time-dependent elastic modulus, CTE and autogenous shrinkage strains are predicted by means of multi-scale analysis. These are realized in the subroutine UEXPAN.

The flowchart of the implementation of the proposed constitutive model is shown in Fig. 4.

4   Numerical modeling and test validation

4.1   Description of full-scale test

The full-scale test refers to the Hong Kong-Zhuhai-Macao (HZM) Link, which is a major infrastructure project, currently under construction. It consists of two parts of a cable stayed bridge, connected by an immersed tunnel. The immersed tunnel consists of 33 elements, varying from 112.5 to 180 m in length, resulting in a total length of 5664 m. Each standard element consists of 8 segments 22.5 m. A typical cross-section of a segment is 37.96 m wide and 11.4 m high, as shown in Fig. 5. The thickness of major parts gives as follows: base slab: 1.5 m, side walls: 1.5 m, inner wall: 0.8 m, and top slab: 1.5 m.
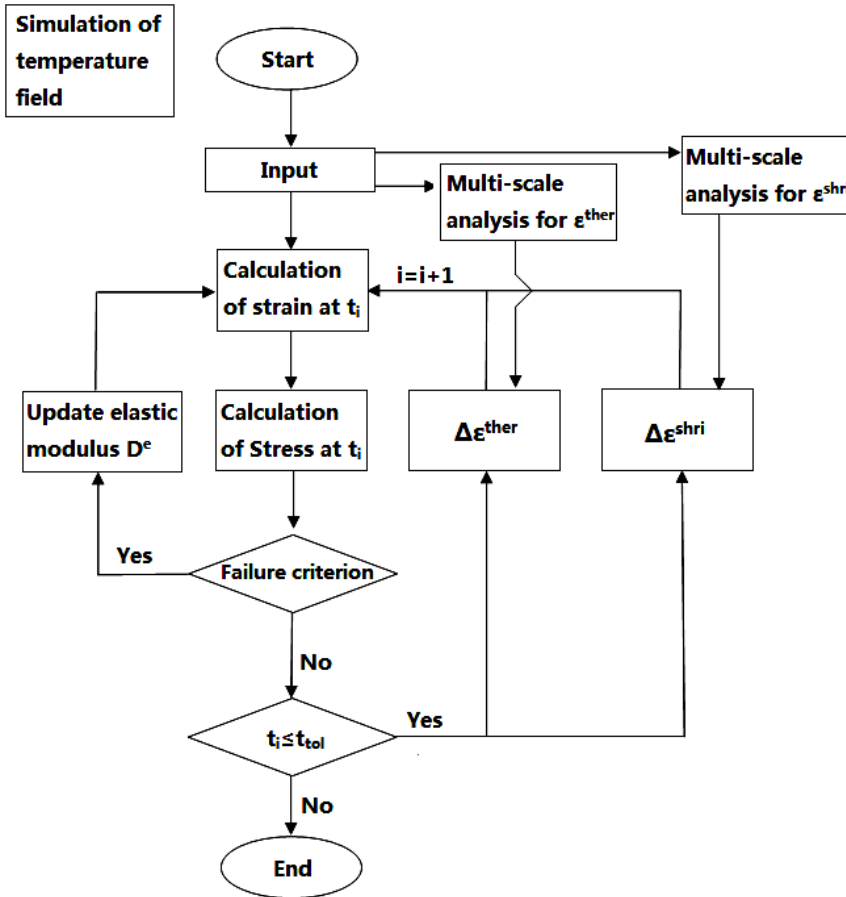
Figure 4: Flowchart of the implementation of the constitutive model.

A full scale segment of 5.8 m length (1/4 of the actual length of the segment) is used in the experimental investigation. During the test, the time-dependent temperature and strains of the central cross-section of the tested segment are monitored through embedded thermocouples and strain gauges. A detailed description of the operation of this test, including the monitoring program, casting, and the curing program is given in [Liu (2013)].
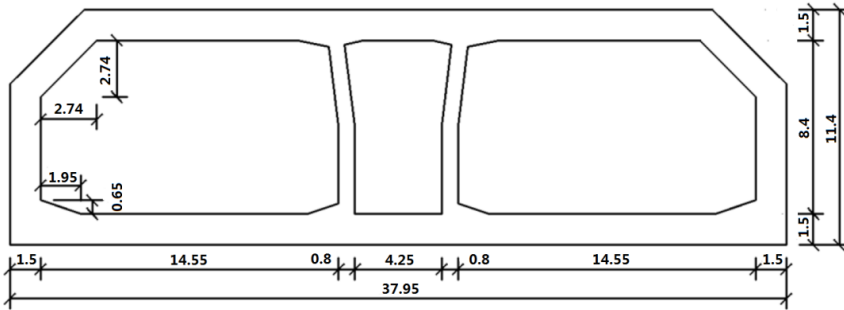
Figure 5: Typical cross-section of a sgement of the immersed tunnel.

4.2 Mix design and material properties

4.2.1 Mix design

High strength concrete (HSC) is used for the tested segment. Its mixture composition is given in Tab. 1. P.O. 42.5, along with the fly ash and blast-furnace slag, represents the cementitious materials. Crushed stone and graded river sand are used as aggregates. Moreover, a commercially available water-reducing admixture (HRWRA) is also used. The chemical composition and the physical properties of the cementitious materials are given in Tab. 2.

Table 1: Mix design of the high strength concrete (kg/m^3)

w/c	Cement	Water	Sand	Coarse agg.	Fly ash	slag	HRWRA
0.34	180	136	740	1105	80	140	3.08

Table 2: Chemical composition of the cementitious materials (%)

	SiO_2	Al_2O_3	Fe_2O_3	CaO	SO_3	K_2O	MgO	f-CaO	Na_2O
Cement	20.95	5.22	5.20	64.12	1.25	0.95	1.46	0.85	-
Fly ash	55.30	22.90	3.18	1.46	0.27	2.73	1.46	-	0.72
slag	34.20	13.39	1.20	38.20	0.28	-	9.02	-	-

4.2.2 Elastic modulus

The detailed description of the process and the results of the laboratory tests on the elastic modulus of the cement paste can be found in the literature [Liu and Liu

(2013)]. Based on the representation of different scales mentioned previously, the finite element discretization of a RVE by means of tetrahedral elements is shown in Fig. 6. Then, the elastic modulus of homogenized concrete at early-age can be calculated by the multi-scale approach described in sub-chapter 3.2, and results are fit, as shown in Fig. 7.
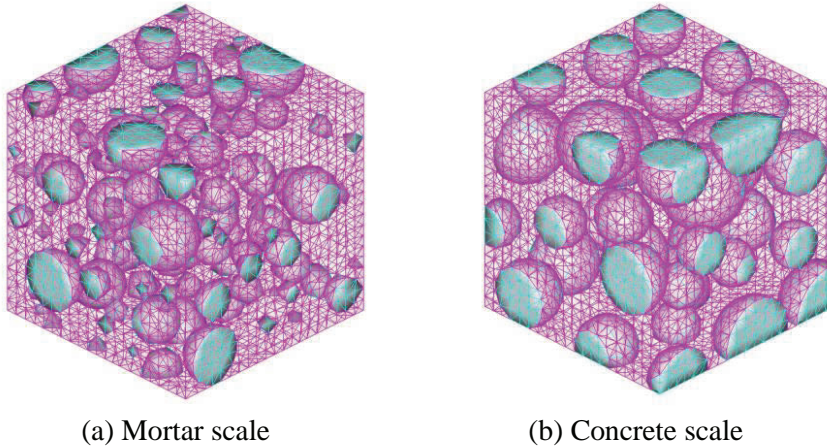

(a) Mortar scale   (b) Concrete scale

Figure 6: Finite element discretization of a RVE.
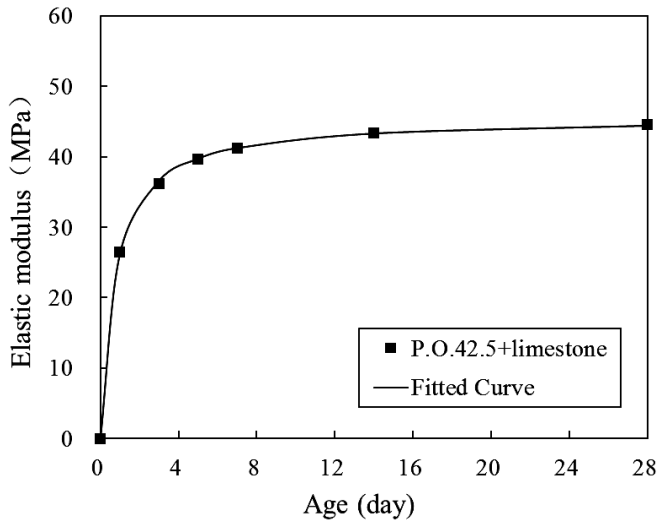
Figure 7: Calculated results and fitted curve for the homogenized elastic modulus.

4.2.3 CTE

The detailed description of the process and results of the laboratory tests on the CTE of cement paste can be seen in the literature [Wyrzykowski and Lura (2013)]. By analogy, the homogenized CTE of concrete at early-age can be calculated by means of the multi-scale approach described in sub-chapter 3.3. The results are fit, as shown in Fig. 8. The process and the validation of this calculation are shown in literature [Liu and Liu (2013)].
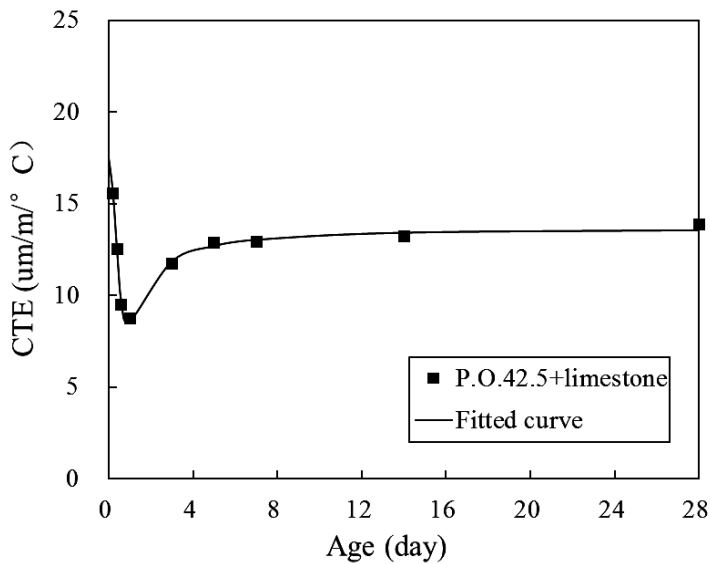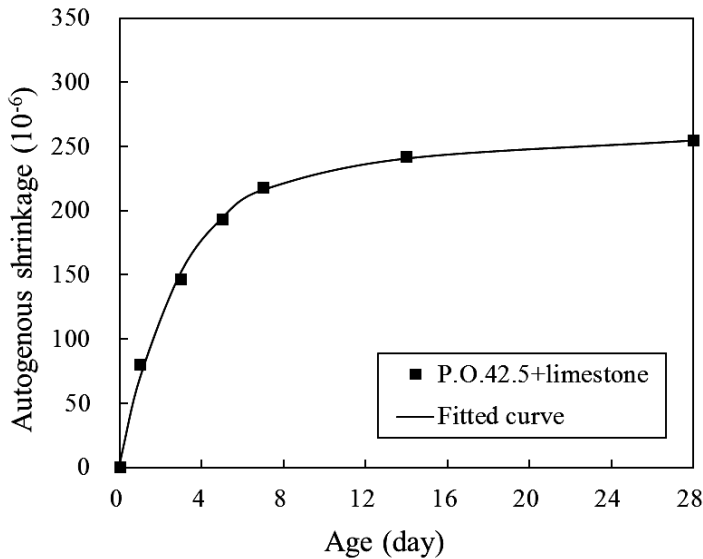

Figure 8: Calculated results and fitted curve for the homogenized CTE.

4.2.4 Autogenous shrinkage strain

For the autogenous shrinkage strain of the cement paste, a laboratory test method conforming to the ASTM C1698-09 (Standard Test Method for Autogenous Strain of Cement Paste and Mortar) is chosen. A detailed description of the process and results can be found in the literature [Liu and Liu (2014)]. The autogenous shrinkage strain of homogenized concrete at early-age can then be calculated by means of the multi-scale approach in sub-chapter 3.4, and results are fit, as shown in Fig. 9. The process and the validation of this calculation are shown in literature [Liu and Liu (2014)].

Figure 9: Calculated results and fitted curve of autogenous shrinkage strain.

4.3 Numerical implementation

4.3.1 Finite element mesh of the tested segment

For both the thermal and the mechanical analyses, the tested segment is discretized with 8-node isoperimetric finite element, as shown in Fig. 10; the element size is set as 0.3 m. The total number of elements is 40173. Stresses and strains are computed at the Gauss integration points inside each element. The coordinate x refers to the horizontal direction of the cross-section, the coordinate y refers to the direction of gravity, and the coordinate z refers to the longitudinal direction.

In the thermal analysis, the temperature field is simulated without considering the action of gravity. In the mechanical analysis, the tested segment is cured with the formwork during the first 3 days, which is defined as step 1. During this period, the formwork carries the weight of the material. The action of gravity is ignored. Thereafter, the formwork is stripped and the segment is exposed to the environment until the end of monitoring. This is defined as step 2, during which the action of gravity is taken into consideration.

4.3.2 Boundary conditions

1. Thermal boundaries
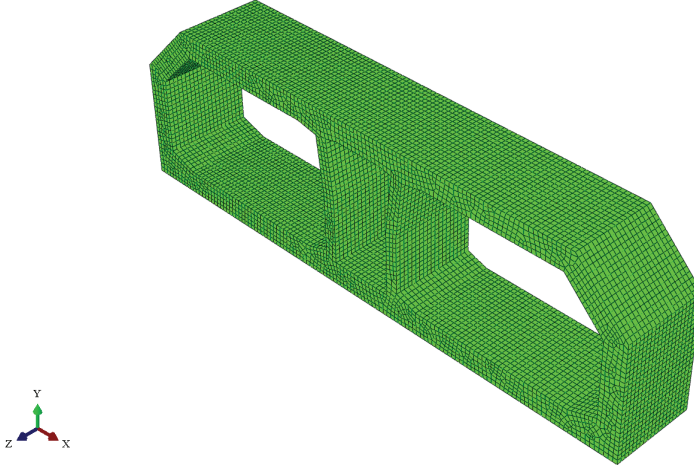
Figure 10: Finite element mesh of the tested segment.

During the simulation, the equivalent coefficients of the heat exchange between the concrete surface and the environment can be obtained by:

$$\chi_{eq} = \frac{1}{\left[\frac{1}{\chi_c} + \sum \left(\frac{h_i}{\lambda_i}\right)\right]}, \quad (W/m^2 \cdot K) \tag{50}$$

In Eq. (50), χ_c is the coefficient of the heat exchange between the concrete surface and the environment, where the heat transfer is occurring, h_i is the thickness of the formwork, and λ_i is the conduction coefficient. In this simulation, χ_{eq} are computed as 9.9 $W/m^2 \cdot K$ for the steel formwork, and as 10.9 $W/m^2 \cdot K$ for the exposed environment.

2. Mechanical boundaries

Since the tested segment is placed on the rigid ground with PTEF (polytetrafluoroethylene) plate between them, the vertical displacement is restrained at all points of the lower surface of the base slab. The friction coefficient between the base slab and the PTEF plate is 0.7, which is simulated by spring elements in two horizontal directions. The stiffness of spring is set as $7 \times 10^4 N/m^2$.

4.4 Model validation

The proposed constitutive model is validated by comparing the results from the analysis at typical positions of the segment with the experiment results. Typical positions of the segment are: the axil angle between the base slab and the inner

wall (DBZQ), the axil angle between the base slab and the side wall (DBCQ), the axil angle between the top slab and the inner wall (TBZQ), the middle section of the base slab (upper surface DBMN and center DBMC), the middle section of the side wall (inner surface CQMN and center CQMC) and the middle section of the top slab (lower surface TBMN and center TBMC), as shown in Fig. 11.
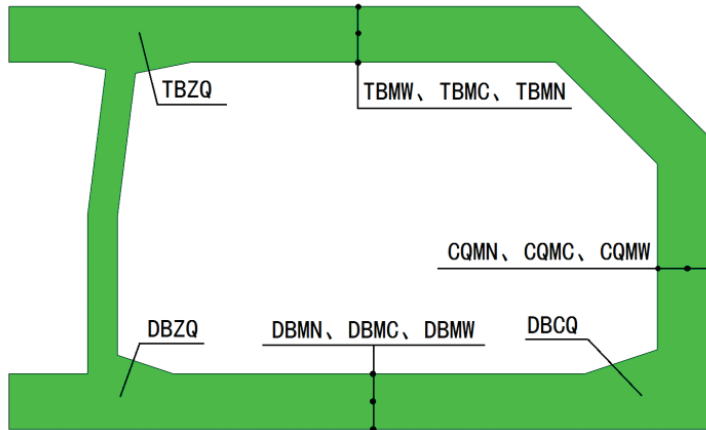

Figure 11: Typical positions of tested segment.

4.4.1   *Temperature development*

Fig. 12 shows the calculated temperature field of the tested segment at day 1.8. It can be seen that the maximum temperature reaches 62.1°.

Firstly, it is noticed that the maximum temperature occurs at the axil angles and at the center of the top slab, the base slab and the side wall. Secondly, it is observed that the temperature in the Z direction is almost constant, which indicates that the temperature varies mainly in the transversal direction rather than in the longitudinal section. Then, four typical positions DBMC, CQMC, TBMC and TBZQ are selected to further investigate the development of the temperature, as shown in Fig. 13.

Taking DBMC as an example, the curve shows a plot of the temperature (°) versus the age of the concrete in days. Along with the time, the temperature increases rapidly to the maximum 60.0° at day 1.9 for the monitored data, the respective maximum obtained from the analysis is 59.5° at day 1.8. Then, the temperature decreases slowly, converging to the ambient temperature. The results at day 14 are 30.3° for monitored data and 32.2° for calculated data. It is seen that the monitored data are slightly lower than the calculated data after the maximum temperature.
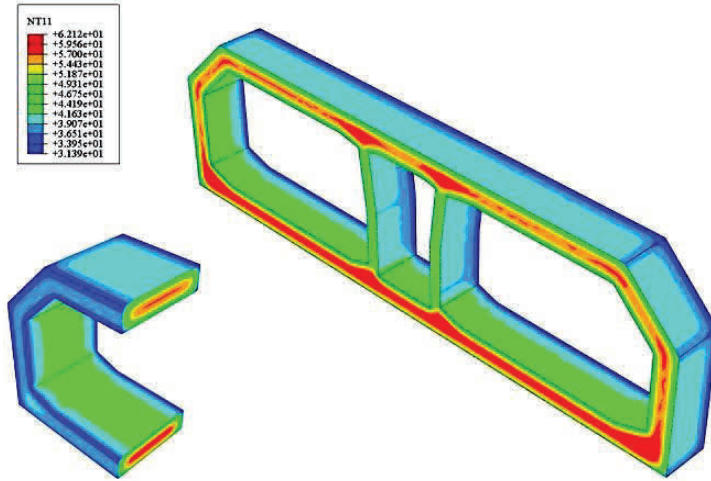
Figure 12: Temperature distributions at day 1.8.

The difference is between 0.3~2.2°. The largest difference occurs at day 8. The reason for this is the underestimation of the heat exchange coefficient in step 2 (see section 4.3.2), when the segment is exposed in air. Nevertheless, a very good correlation between the monitored and the calculated data is noticed. The square of the correlation coefficient is as high as 0.989. For CQMC, the maximum temperature is 60.8° at day 1.5 for monitoring, and 58.3° at the same time for calculated data. The square of the correlation coefficient is 0.966. For TBMC, the maximum temperature is 61.3° at day 1.5 for monitored data, 57.8° at day 1.6 for calculated data. The square of the correlation coefficient is 0.947. For DBZQ, the maximum temperature is 60.5° at day 1.8 for monitored data, and 61.3° at day 2.3 for calculated data. The square of the correlation coefficient is 0.963. Therefore, it can be concluded that the proposed model is well suited for the analysis of the temperature field.

4.4.2 Strain development

The presentation of the results from the analysis of the strain field consists of two parts: the field of the strains in the x direction and in the z direction, respectively. Fig. 14 shows the strain field in the x direction at day 1.8, when the maximum tensile strain occurs both in step 1 and step 2. It is noticed that the strain in the x direction is relatively uniformly distributed, and that the strain in the base slab is slightly smaller than in the other parts of the structure. Fig. 15 shows the strain field in the z direction at day 1.0, when the maximum tensile strain occurs. It is
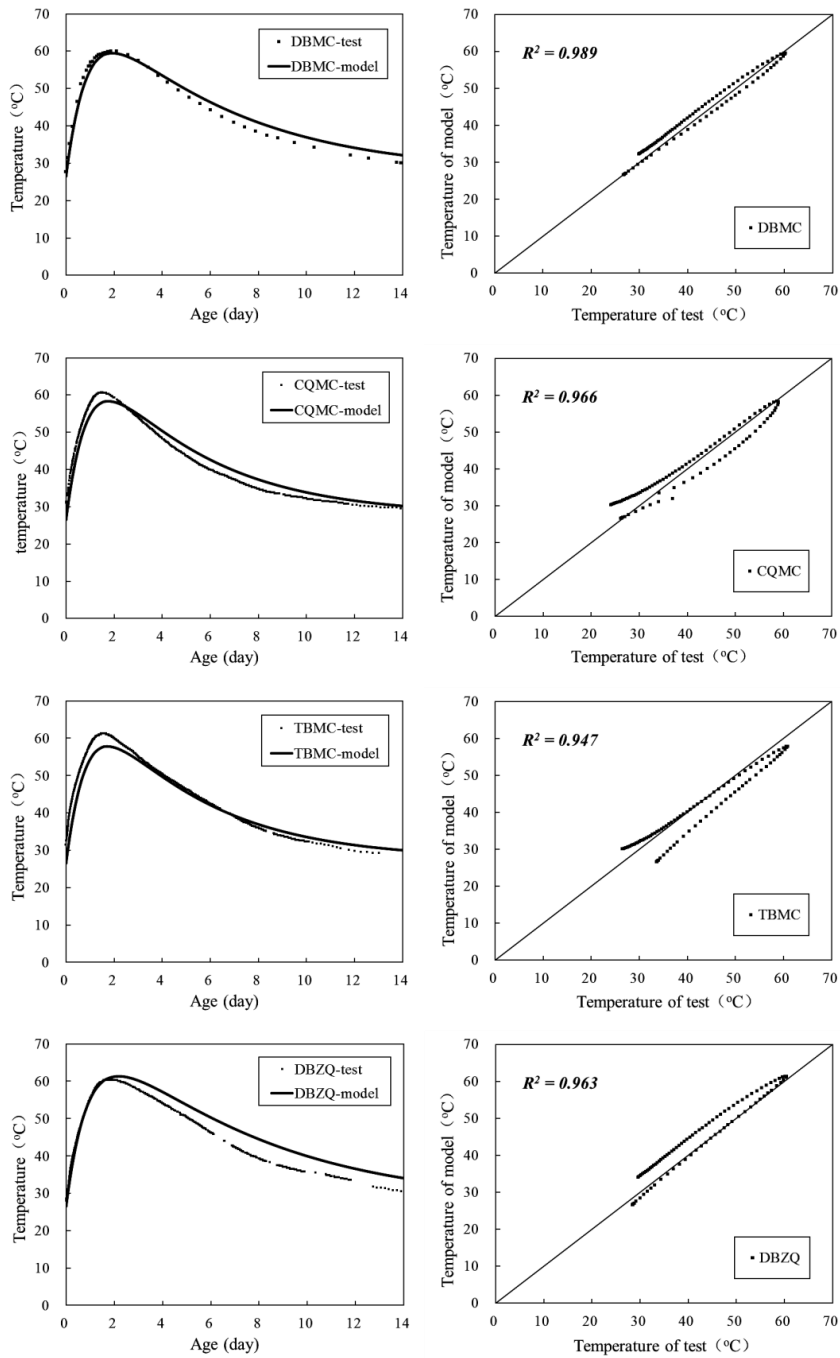
Figure 13: Comparison of monitored data and calculated data.

observed that the strain in the z direction at the edges of the segment is larger than in the middle, especially at the outer edges of the base slab. In the following, three typical parts of this segment: the base slab, the side wall, and the top slab are selected to further show the development of strain.
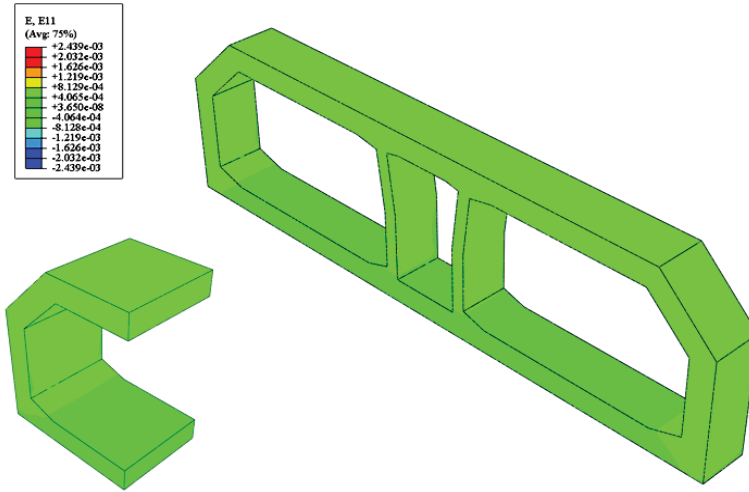

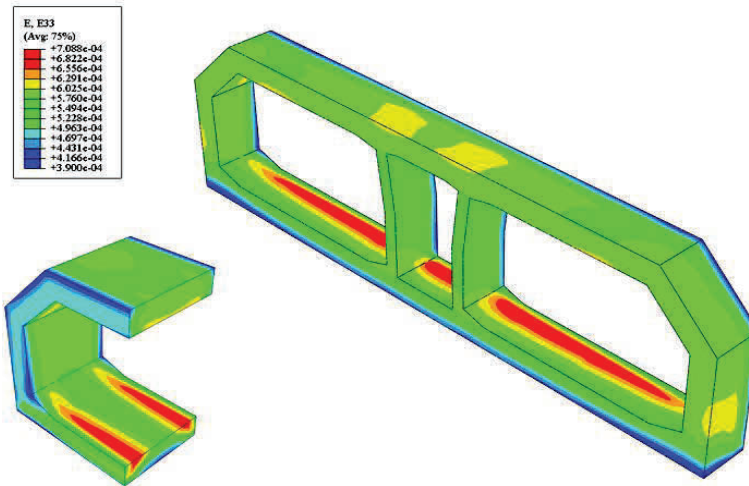Figure 14: Strain field in the x direction at day 1.8.

Figure 15: Strain field in the z direction at day 1.0.

1. Middle section of the base slab

Two strain gauges are placed at the center (DBMC) and the inner surface (DBMN) of the base slab, monitoring the strain ($\mu\varepsilon$ refers to 10^{-6}) in the x direction. Fig. 16 shows a comparison of monitored data and calculated data for the strain in the x direction, in the middle section of the base slab, both at the DBMC and the DBMN. Tensile strain is defined as positive, and compressive strain as negative.
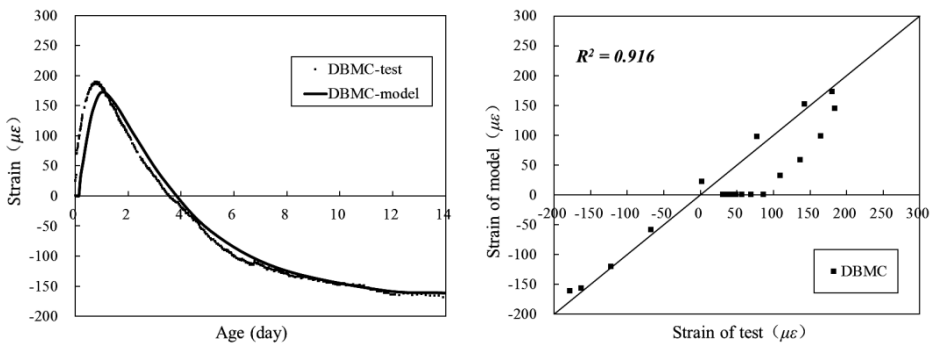
(a) DBMC
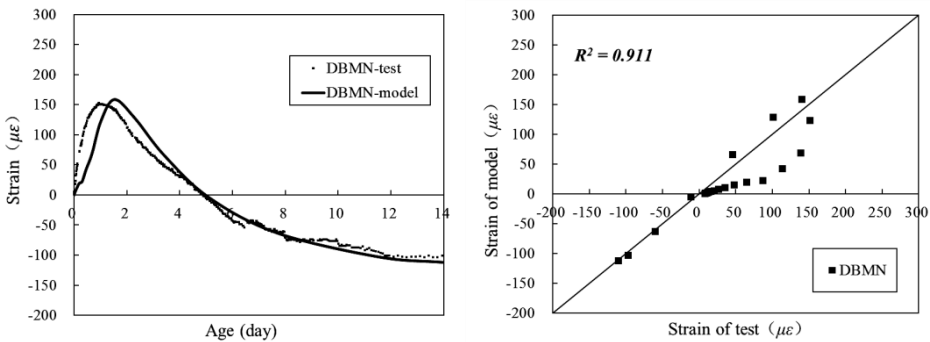
(b) DBMN

Figure 16: Comparison of monitored data and calculated data for the strain in the x direction in the middle section of the base slab.

On the one hand, Fig. 16 shows that the strain follows the trend of a rapid increase of the tensile strain up to its maximum, followed by a gradual decrease to zero before transforming to compressive strain. This can be explained by the fact that, at the beginning, the temperature is rising rapidly with high CTE, whereas the autogenous shrinkage strain is small. Hence, dominated by thermal expansion, the strain is a tensile strain. As the temperature and CTE decreases with time, thermal

contraction occurs, together with the development of autogenous shrinkage strains, resulting in the change toward compressive strain. It is noticed that the correlation between the monitored data and the calculated data for both the DBMC and the DBMN is good. The square of the correlation coefficient is as high as 0.916 and 0.911, respectively. This validates the effectiveness of the proposed constitutive model for the analysis of the strain field.

On the other hand, both at the DBMC and the DBMN, the maximum of the tensile strain is reached at about 1 day, however, at the DBMC, the maximum of the tensile strain, $172.9\mu\varepsilon$, is greater than the one at the DBMN, $158.0\mu\varepsilon$. The change from a tensile to a compressive strain occurs faster at the DBMC than at the DBMN. The final value for the DBMC is $-161.4\mu\varepsilon$, whereas for the DBMN, it is $-111.9\mu\varepsilon$. The reason for this difference is that the DBMC is located in the center position, while DBMN is located at the inner surface which is not covered by the formwork. For this reason, in this simulation, the constraint at the DBMC is stronger than that at the DBMN.

2. Middle section of the side wall

Two strain gauges are placed in the center (CQMC) and at the inner surface (CQMN) of the side wall, which monitor the stain in the z direction. Fig. 17 shows a comparison of monitored data and calculated data for the strain in the z direction, in the middle section of the side wall, both at the CQMC and the CQMN. The development of the strain shows the same trend as in the middle section of the base slab. A good correlation is noticed between monitored data and calculated data for both the CQMC and the CQMN. The square of the correlation coefficient is as high as 0.972 and 0.984, respectively.

It is seen that, at the CQMC and the CQMN, the maximum tensile strain occurs at day 1. The maximum tensile strain at the CQMC, $152.0\mu\varepsilon$, is close to the one at the CQMN, $155.7\mu\varepsilon$. Then, for both the CQMC and the CQMN, the tensile strain changes to a compressive strain around day 4, finally reaching a value of about $-165\mu\varepsilon$. It is concluded that the side wall dilates or contracts uniformly in the z direction, which is the consequence of the same constraint on the CQMC and the CQMN in the z direction.

3. Middle section of the top slab

Two strain gauges are placed in the center (TBMC) and at the inner surface (TBMN) of the top slab, which monitor the stain in the x direction. Fig. 18 shows a comparison of monitored data and calculated data for the strain in the x direction, in the middle section of the top slab, both at the TBMC and the TBMN. The development of strain shows the same trend with the middle section of base slab too. And, a good correlation also can be noticed between monitored data and calculated
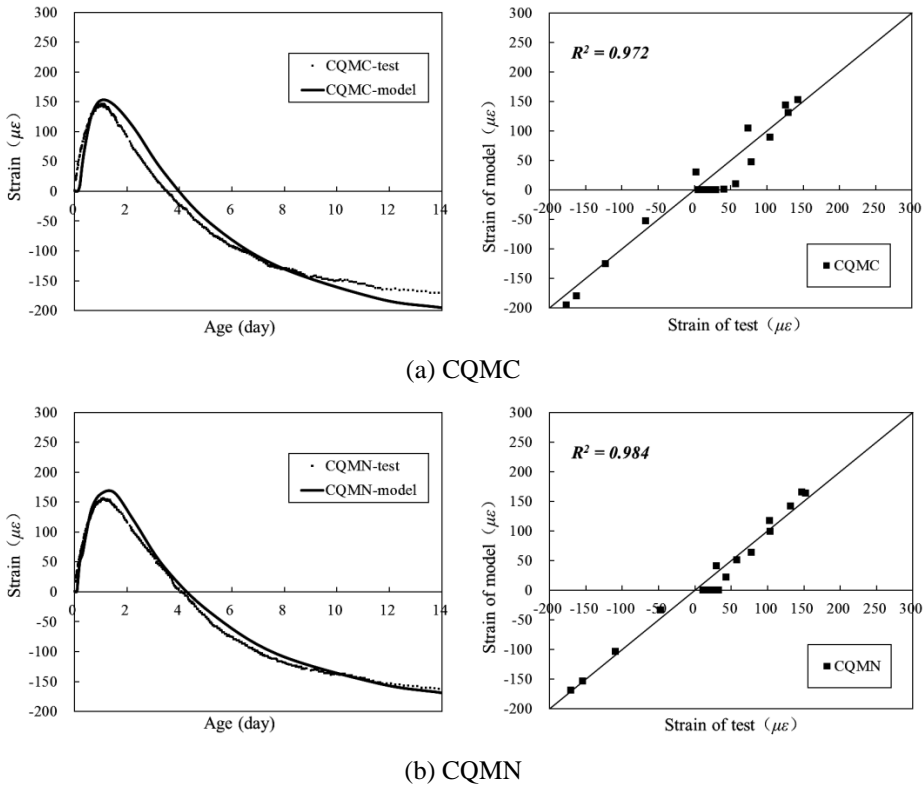
(a) CQMC

(b) CQMN

Figure 17: Comparison of monitored data and calculated data for the strain in the z direction in the middle section of the side wall.

data for both at the TBMC and the TBMN. The square of the correlation coefficient is as high as 0.980 and 0.988.

It is observed that, both the TBMC and the TBMN reach the maximum tensile strain within 24 hours. However, the maximum of the tensile strain at the TBMN, $161.0\mu\varepsilon$, is greater than that at the TBMC, $142.0\mu\varepsilon$. The strain at the TBMC changes its sign from tensile to compressive faster than the strain at the TBMN. The final value is $-178.5\mu\varepsilon$, and the one of the latter is $-162.1\mu\varepsilon$. The reason for this is that the dissipation of heat at the TBMN is poor because of the steel formwork that has a smaller heat-exchange coefficient of $9.9\ W/m^2 \cdot K$. Therefore, the tensile strain which is cause predominantly by thermal expansion is larger. In step 2, when the TBMN is exposed to the air, the heat-exchange coefficient is 10.9 $W/m^2 \cdot K$, and the constraint on the TBMC is stronger than the TBMN.
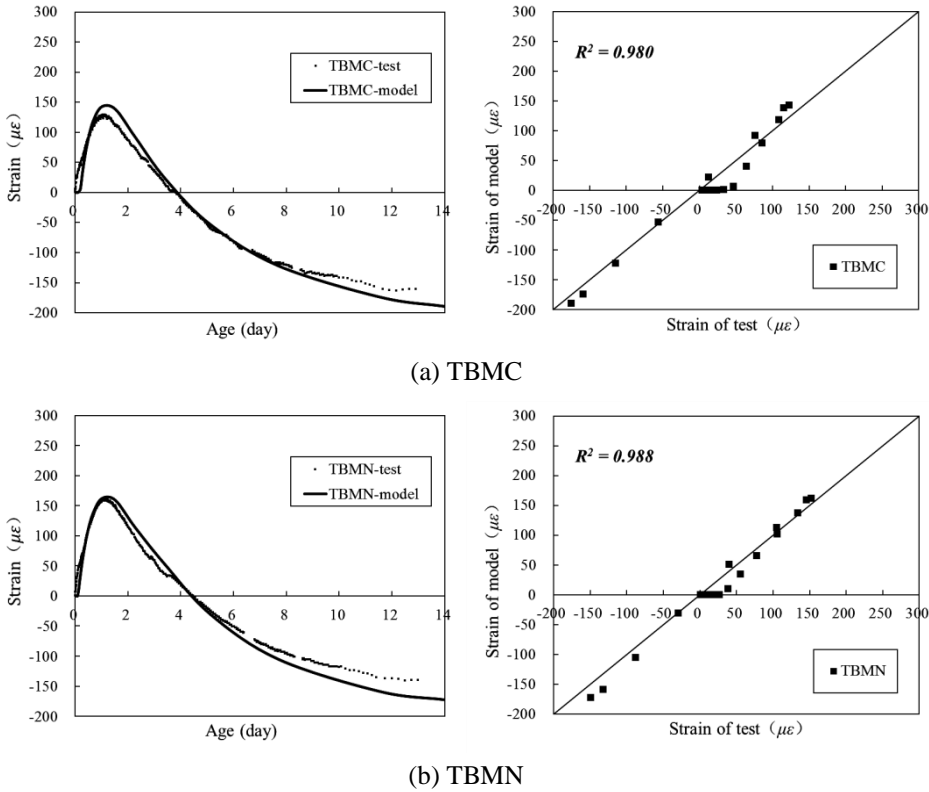
(a) TBMC

(b) TBMN

Figure 18: Comparison of monitored data and calculated data for the strain in the x direction in the middle section of the top slab.

5 Discussion

5.1 Stress development

In step 1, the maximum tensile stress in the x direction occurs at day 2.3. It is concentrated on the surface of the axil angles, as shown in Fig. 19. In the z direction, the maximum tensile stress also occurs at day 2.3. However, it is distributed along the outer edge of the side wall and the top slab, as shown in Fig. 20. This can be explained by the exothermic nature of hydration which leads to the formation of temperature gradients, especially at the axil angles. These gradients and the resulting non-uniform thermal deformations inside the element, together with the autogenous shrinkage deformation, are responsible for the buildup of stresses at the surface.

In step 2, the maximum tensile stress in the x direction occurs at day 14. It is mainly
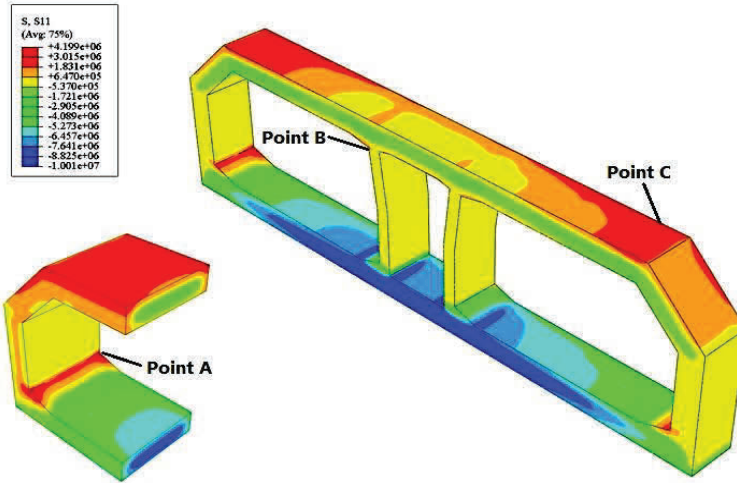
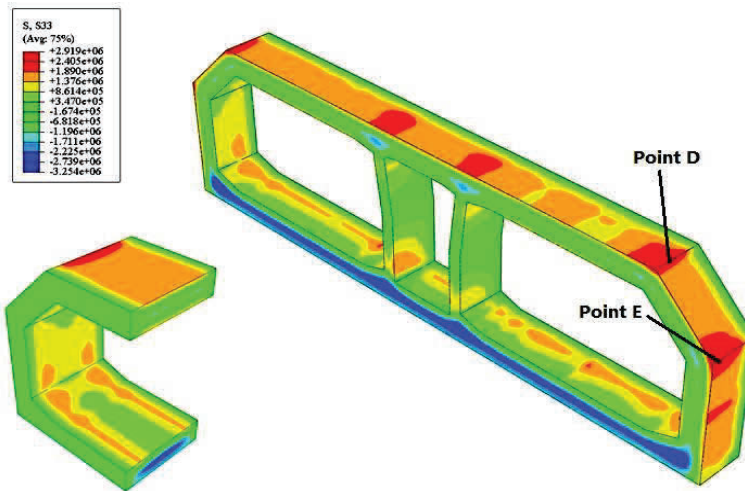Figure 19: Stress field in the x direction at day 2.3 in step 1.

Figure 20: Stress field in the z direction at day 2.3 in step 1.

concentrated on the TBMN, and at the outer surface of the top slab at the inner wall, as shown in Fig. 21. It can be explained by the fact that the top slab carries its weight after the removal of the formwork in step 2. In the z direction, the maximum tensile stress occurs at day 3, as shown in Fig. 22. The stress in this direction decreases since day 2.3 in step 1. This is because the action of gravity in the z

direction is nearly ignored, compared with the action of thermal and autogenous shrinkage deformation.
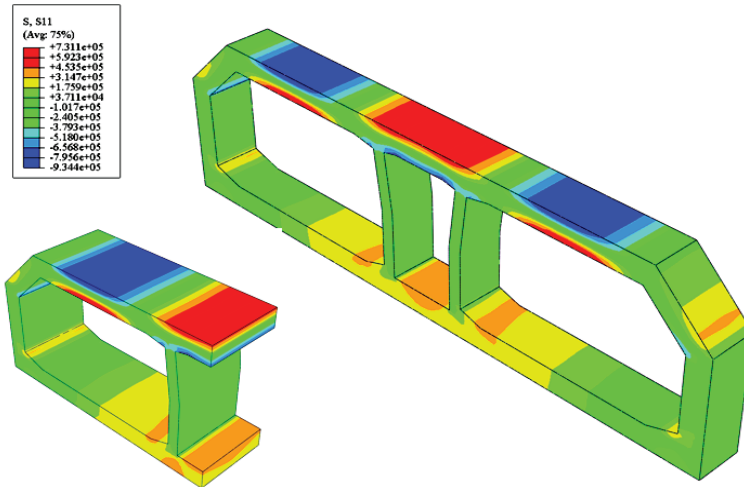

Figure 21: Stress field in the x direction at day 14 in step 2.
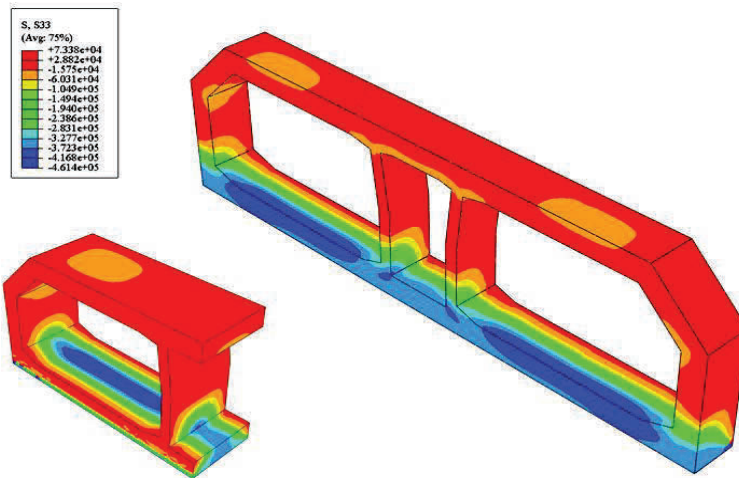

Figure 22: Stress field in the z direction at day 3 in step 2.

Then, two typical points: point A and D (as shown in Fig. 19 and Fig. 20) are selected to further show the development of stress, which refer to the stress in the x direction and the z direction, as shown in Fig. 23.
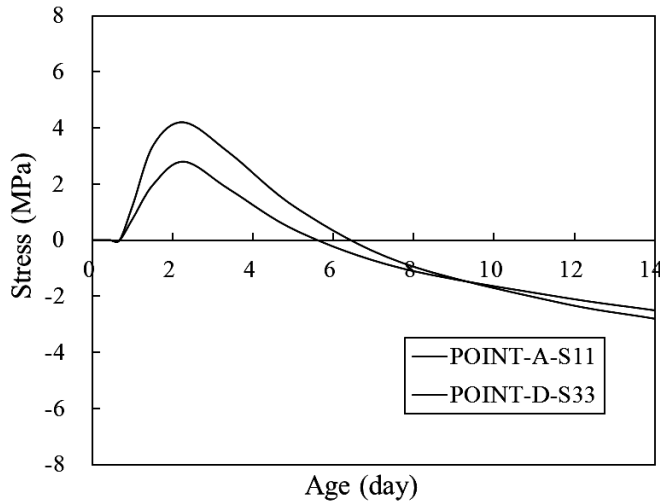
Figure 23: Development of stress at point A and point D.

The tensile stress is defined as positive, and the compressive stress as negative. Fig. 23 shows that, the tensile stress increases rapidly to its maximum of 4.2MPa at day 2.3. Then, it decreases gradually to zero at day 5.5, and changes to a compressive stress. The final value at day 14 is -2.8MPa. The ultimate tensile strength of the concrete used in this test is 2.3MPa, as obtained from laboratory tests on the mechanical properties, while the maximum tensile stress at point A is 4.2MPa. Thus, it is concluded that this area cracks.

While for the stress in the z direction at point D, the tensile stress increases rapidly to its maximum of 2.9MPa at day 2.3 at the beginning. Then, it decreases gradually to zero at day 5.2, and changes to compressive stress. The final value at day 14 is -2.2MPa. Thus, the maximum stress exceeds the ultimate tensile strength 2.3MPa. It is concluded that this area cracks, which is in accord with the engineering phenomenon of leakage due to the vertical cracks at side wall.

5.2   *Influence of materials*

It is worth mentioning that the proposed constitutive model is based on a multi-scale approach using asymptotic expansion theory. Thus, the hydration process of cement and the random distribution of aggregates are taken into consideration. In this section, different kinds of cement and aggregate are taken into consideration, to obtain a combinatorial optimization of these materials.

5.2.1 Cement

In this section, the influence of the type of the cement on the development of strain at point A and D (see Fig. 19 and Fig. 20) is investigated. The following cements are considered: P.O.42.5, P.II.42.5, and P.II.52.5. According to the scale representation mentioned in chapter 2, different kinds of cements along with fly ash and blast-furnace slag are used as cementitious materials. 5-20mm graded and crushed limestone is used as the coarse aggregate and 0.25-1.0mm graded river sand as the fine aggregate. The finite element discretization of the RVE by means of tetrahedral elements is shown in Fig. 6. The elastic modulus, CTE, and the autogenous shrinkage strain of homogenized concrete at early age can be calculated by the multi-scale approach described in sub-chapter 3.2 to 3.4. The results are fitted, as shown in Fig. 24 to Fig. 26.
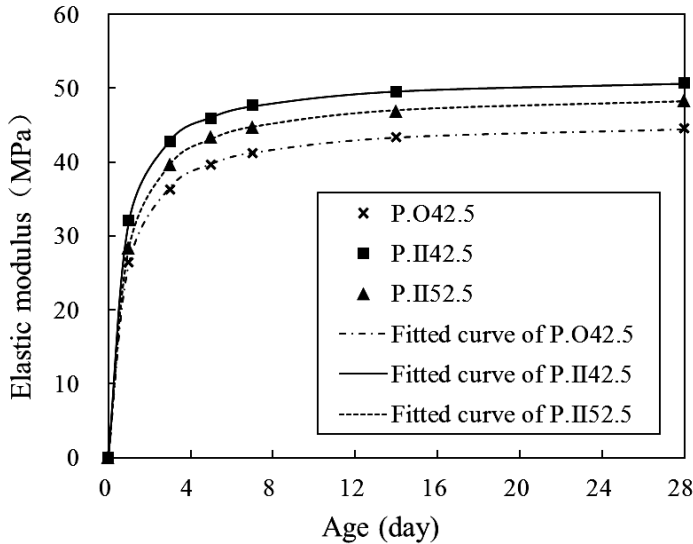
Figure 24: Calculated results and fitted curves for the elastic modulus with different cements.

Fig. 27 shows a comparison of the stress in the x direction at point A and strain in the z direction at point D with different cements (see Fig. 19 and Fig. 20). Firstly, the curves show the same trend. Secondly, the maximum tensile stress for P.O.42.5 is obviously smaller than that for P.II.42.5, and the maximum tensile stress for P.II.52.5 falls in between the two. At day 14, the magnitudes of final compressive stress for P.O.42.5, P.II.42.5 and P.II.52.5 are related to one another in the same way. The CTE for the three different kinds of cement are characterized
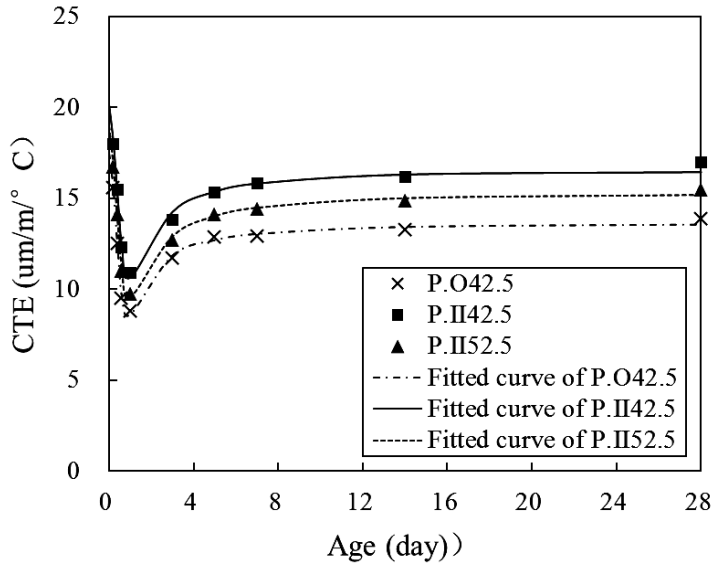
Figure 25: Calculated results and fitted curves for the homogenized CTE with different cements.
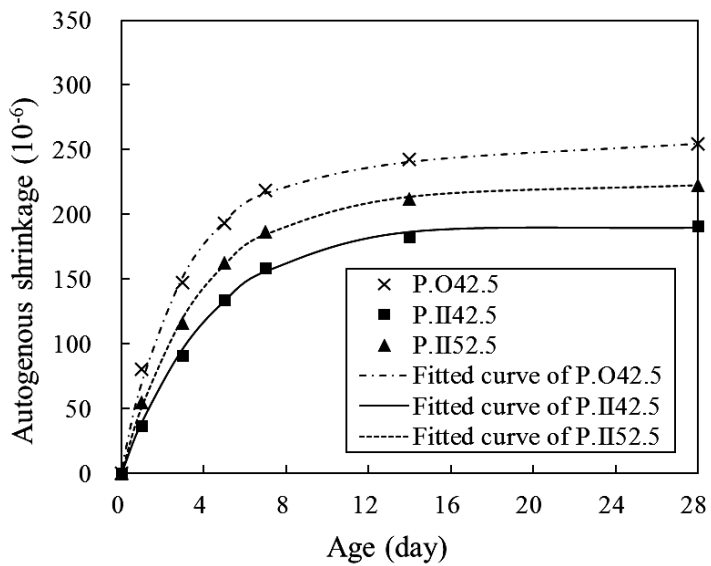

Figure 26: Calculated results and fitted curves for the autogenous shrinkage strain with different cements.
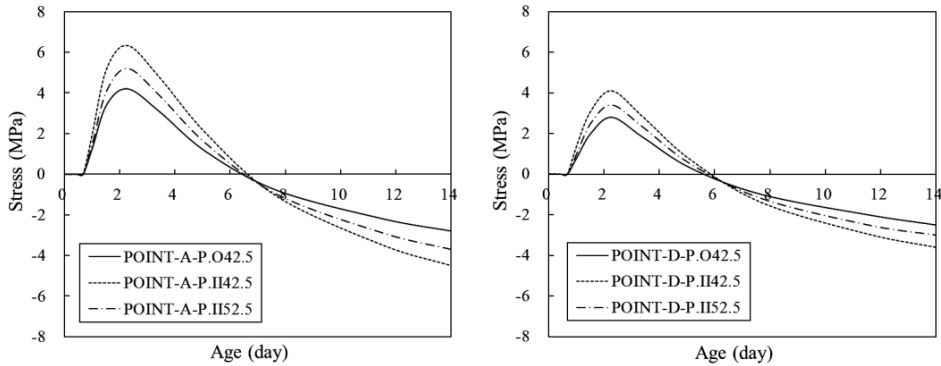
Figure 27: Comparison of the stress in the x direction at point A and the stress in the z direction at point D with different cements.

by P.II42.5> P.II52.5> P.O42.5, as shown in Fig. 25. That is to say, the CTE is the dominant factor in this simulation, and it is concluded that the thermal stress is the main contribution to the total stress. Thus, from the above discussion all above, it is seen that the type of the cement has a strong influence on the development of stress and that P.O.42.5 cement is a better choice for the purpose of control of cracking in engineering practice.

5.2.2 Aggregate

In this section, the influence of the type of the aggregate is investigated by means of a comparative study on the development of stress in x direction at point A and stress in z direction at point D. Crushed and graded siliceous aggregate (quartzite), igneous aggregate (granite), and calcareous aggregate (limestone) are chose for the comparison of their influence. Mechanical and thermal properties of these aggregates are shown in Tab. 3.

Table 3: Mechanical and thermal properties of coarse aggregate [Bazant and Kaplan (1996)].

Type	E (GPa)	Poisson's ratio	CTE(um/m/°C)
Quartzite	27.9-69.3	0.17-0.36	10.3
Granite	24.8-61.1	0.12-0.27	6.8
Limestone	29.4-84.2	0.18-0.35	5.5

According to the scale representations mentioned in chapter 2, cement P.O. 42.5,

along with fly ash and blast-furnace slag, are used as cementitious materials. Different kinds of 5-20mm coarse aggregate are used. 0.25-1.0mm graded river sand is used as fine aggregate. Then, the homogenized elastic modulus, the CTE and the autogenous shrinkage strain are calculated by the multi-scale approach proposed in sub-chapter 3.2 to 3.4. The results are fitted, as shown in Fig. 28 to 30.
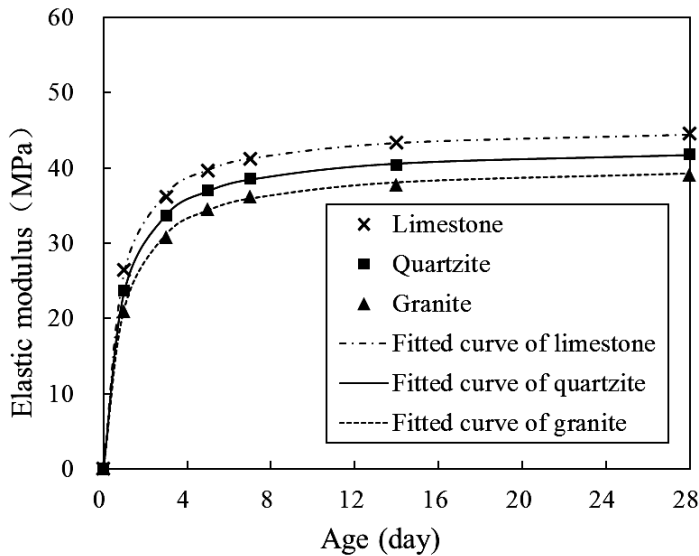

Figure 28: Calculated results and fitted curves for the elastic modulus with different aggregates.

Fig. 31 shows a comparison of the stress in the x direction at point A and the stress in the z direction at point D with different aggregates. The thermal stress is the dominant part of the total stress. The magnitude of the CTE for the different aggregates conform to quartzite> granite>limestone as shown in Fig 5.12. The maximum tensile stress with calcareous aggregate (limestone) is obviously smaller than concrete with siliceous aggregate (quartzite), while concrete with igneous aggregate (granite) falls in between these two. At day 14, the final compressive stress in concrete with limestone, quartzite and granite is analogous to the one for tensile stress. Thus, it is concluded that the type of the aggregate also has an important influence on the development of stress, and limestone is a better choice in engineering practice for the purpose of control of cracking.
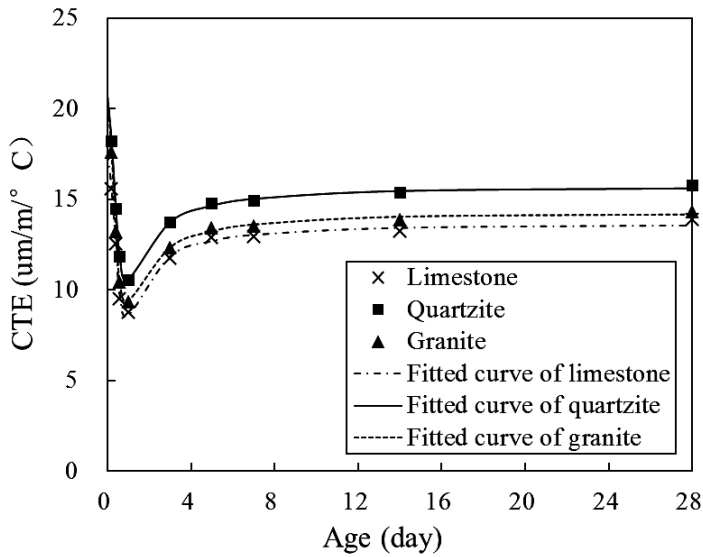
Figure 29: Calculated results and fitted curves for the homogenized CTE with different aggregates.
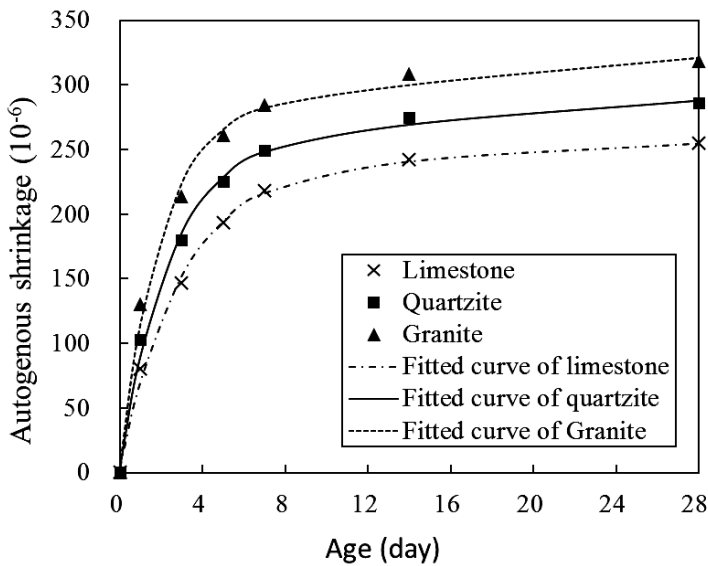

Figure 30: Calculated results and fitted curves for the autogenous shrinkage strain with different aggregates.
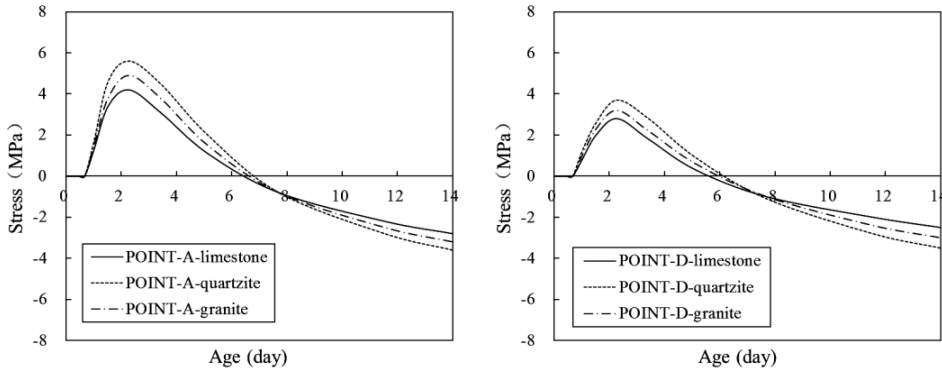
Figure 31: Comparison of the stress in the x direction at point A and the stress in the z direction at point D with different aggregates.

6 Summary and Conclusions

In this research, a nonlinear viscoelastic constitutive model considering time-dependent properties and volumetric deformation was proposed. The elastic modulus, the CTE, and the autogenous shrinkage strain were computed by means of multi-scale analysis. The obtained constitutive model was implemented in finite element software. Then, a comprehensive study, comparing the results from numerical simulation and a full scale experiment of HZM immersed tunnel, was conducted considering the temperature field and the strain field. In this way, the proposed constitutive model was validated. Therefore, the stress field in the structure was determined. Different kinds of cement and aggregate were considered in order to obtain a combinatorial optimization of materials. The following conclusions can be drawn:

1. Thermal analysis has shown that the temperature varies mainly at the transversal section and much less in the longitudinal section. The maximum temperature occurs at day 1.8, at the axil angles and in the center of the top slab, the base slab and the side wall. The temperature of the different parts of the segment increases rapidly to the maximum. Thereafter, it decreases slowly, converging to the ambient temperature.

2. In the strain analysis, the maximum tensile strain in the x direction occurs at day 1.8, both in step 1 and step 2, and it is basically uniformly distributed. The maximum tensile strain in the z direction occurs at day 1.0, primarily appears along the edges of the base slab. The development of strains is characterized by a rapid increase to the maximum, followed by a gradual decrease to zero, before becoming

a compressive strain.

3. Stress analysis has shown that, the maximum tensile stress in the x direction in step 1 occurs at day 2.3. It occurs mainly on the surface of the axil angles. In step2, it occurs at day 14 at the TBMN, and at the outer surface of the top slab at inner wall. In the z direction, the maximum tensile stress in step 1, as well as step2 occurs at day 2.3. It is primarily distributed along the outer edge of the side wall and the top slab. In the analysis of the development of stress, two typical points (A and D) were chosen for the preventative of the results. When the maximum tensile stress exceeds the ultimate tensile strength, the concrete is cracking.

4. For the purpose of optimizing of the material properties, different kinds of cement and aggregate were taken into account. From the results, it is concluded that the type of cement and aggregate has an important influence on the development of stress. P.O.42.5 cement and limestone appears to be a good choice for control of cracking in engineering practice

In the proposed model, the mechanical and thermal properties of the cement paste are obtained directly from experiments on the cement paste scale, which are standardized and highly precise from the set. Thus, a completely cross-scale research from the cement paste to the macro structure of concrete is realized, avoiding a variety of non-standardized and highly specialized test methods for concrete. In the future, improvements of the model as regards consideration of the cement hydration will be made focus on the mixture characteristics and the cement chemistry. Moreover, the optimization of material will be conducted on more factors, such as constituents and their proportion in cementitious materials, the additive, the w/c, the curing temperature and the humidity, etc.

References

Acker, P.; Ulm, F. J. (2001): Creep and shrinkage of concrete: Physical origins and practical measurement. *Nuclear Engineering and Design*, vol. 20, no. 2, pp. 143-158.

Amin, M. N.; Kim, J. S.; Lee, Y. (2009): Simulation of the thermal stress in mass concrete using a thermal stress measuring device. *Cement and Concrete Research*, vol. 39, no. 3, pp. 154–164.

Azenha, M.; Faria, R. (2009): Identification of early-age concrete temperatures

and strains: Monitoring and numerical simulation. *Cement and Concrete Composites*, vol. 31, no. 6, pp. 369–378.

Ballim, Y.; Graham, P. C. (2004): Early-age heat evolution of clinker cements in relation to micro-structure and composition implications for temperature development in large concrete elements. *Cement and Concrete Composites*, vol. 26, no. 5, pp. 417–426.

Barcelo, L.; Boivin, S. (2001): Early age shrink-age of concrete: Back to physical mechanisms. *Concrete Science and Engineering*, vol. 3 , no. 10, pp. 85 – 91.

Bazant, Z. P. (1970): Delayed thermal dilatations of cement paste and concrete due to mass transport. *Nuclear Engineering and Design*, vol. 14, no. 2, pp. 308–318.

Bazant, Z. P.; Kaplan, M. F. (1996): *Concrete at High Temperatures: Material Properties and Mathematical Models*. London: Longman (Addison-Wesley).

Bentz, D. P. (2008): A review of early-age properties of cement-based materials. *Cement and Concrete Research*, vol. 38, no. 2, pp. 196-204

Bernard, O.; Ulm, F. J.; Lemarchand, E. (2003): A multiscale micromechanics-hydration model for the early-age elastic properties of cement-based materials. *Cement and Concrete Research*, vol. 33, no. 9, pp. 1293-1309.

Bjøntegaard, O.; Hammer, T. A. (2004): On the measurement of free deformation of early age cement paste and concrete. *Cement and Concrete Composites*, vol. 26, no. 5, pp. 427–435.

Bohm, H. J.; Han, W.; Eckschlager, A. (2004): Multi-inclusion unit cell studies of reinforcement stresses and particle failure in discontinuously reinforced ductile matrix composites. *CMES: Computer Modeling in Engineering & Sciences,* vol. 5, no. 1, pp. 5-20.

Briffaut, M.; Benboud, F.; Torrenti, J. M. (2011): Numerical analysis of the thermal active restrained shrinkage ring test to study the early age behavior of massive concrete structures. *Engineering Structures,* vol. 33, pp. 1390–1401.

Cao, C.; Cheung, M. S. (2013): Modeling of interaction between corrosion-induced concrete cover crack and steel corrosion rate. *Corrosion Science*, vol. 69, pp. 97–109.

Chu, I.; Kwon, S. H. (2012): Estimation of temperature effects on autogenous shrinkage of concrete by a new prediction model. *Construction and Building Materials*, vol. 35, pp. 171–182.

Cui, J. Z.; Shin, T. M.; Wang, Y. L. (1999): The two-scale analysis method for bodies with small periodic configurations. *Structural Engineering and Mechanics,* vol. 7, no. 6, pp. 601-614.

Dong, L.; Atluri, S. N. (2012): Development of 3D T-Trefftz Voronoi cell finite

elements with/without spherical voids &/or elastic/rigid inclusions for micromechanical modeling of heterogeneous materials. *CMC: Computers Materials and Continua*, vol. 29, no. 2, pp. 169-211.

Dong, L.; Atluri, S. N. (2012): T-Trefftz Voronoi cell finite elements with elastic/rigid inclusions or voids for micromechanical analysis of composite and porous materials. *CMES: Computer Modeling in Engineering & Sciences*, vol. 83, no. 2, pp. 183-219.

Dong, L.; Atluri, S. N. (2013): SGBEM Voronoi Cells (SVCs), with embedded arbitrary-shaped inclusions, voids, and/or cracks, for micromechanical modeling of heterogeneous materials. *CMC: Computers, Materials & Continua*, vol. 33, no. 2, pp. 111-154.

Dong, L.; Gamal, S. H.; Atluri, S. N. (2013): Stochastic Macro Material Properties, Through Direct Stochastic Modeling of Heterogeneous Microstructures with Randomness of Constituent Properties and Topologies, by Using Trefftz Computational Grains (TCG). *CMC: Computers, Materials & Continua*, vol. 37, no. 1, pp. 1-21.

Du, C. B.; Jiang, S. Y.; Qin, W.; Zhang, Y. M. (2011): Numerical analysis of concrete composites at the meso-scale based on 3D reconstruction technology of X-ray CT images. *CMES: Computer Modeling in Engineering & Sciences*, vol. 81, no. 3, pp. 229-247.

Feng, Y. P., Cui, J. Z. (2004): Multi-scale analysis and FE computation for the structure of composite materials with small periodic configuration under condition of coupled thermo-elasticity. *International Journal for Numerical Methods in Engineering*, vol. 60, no. 11, pp. 1879-1910.

Gawin, D.; Pesavento, F.; Schrefler, B. A. (2006): Hygro-thermo-chemo-mechanical modelling of concrete at early ages and beyond Part I: hydration and hygro-thermal phenomena. *International Journal for Numerical Methods in Engineering*, vol. 67, no. 3, pp. 299-331.

Ghabezloo, S. (2011): Micromechanics analysis of thermal expansion and thermal pressurization of a hardened cement paste. *Cement and Concrete Research*, vol. 41, no. 5, pp. 520-532.

Gawin, D.; Pesavento, F.; Schrefler, B. A. (2006): Hygro-thermo-chemo-mechanical modelling of concrete at early ages and beyond Part II: shrinkage and creep of concrete. *International Journal for Numerical Methods in Engineering*, vol. 67, no. 3, pp. 332-363.

Hellmich, C. (1999): *Shotcrete as part of the new Austrian tunneling method: From thermo-chemo-mechanical material modeling to structural analysis and safety assessment of tunnels*: Doctoral Thesis, Vienna University of Technology.

Hellmich, C.; Ulm, F.; Mang, H. (1999): Consistent linearization in finite element analysis of coupled chemo-thermal problems with exo-prendothermal reactions. *Computational Mechanics*, vol. 24, no. 238, pp. 244-253.

Holt, E. E.; Leivo, M. T. (2006) Cracking risk associated with early age shrinkage. *Cement and Concrete Composites*, vol. 26, no. 5, pp. 521–530.

Ilc, A.; Turk, G. (2009): New numerical procedure for the prediction of temperature development in early age concrete structures. *Automation in Construction*, vol. 18, pp. 849 –855.

Idiart, A.; Bisschop, J. (2012): A numerical and experimental study of aggregate-induced shrinkage cracking in cementitious composites. *Cement and Concrete Research*, vol. 42, no. 2, pp. 272– 281.

Jensen, O. M.; Hansen, P. F. (1995): A dilatometer for measuring autogenous deformation in hardening Portland cement paste. *Materials and Structures*, vol. 28, no. 7, pp. 69–76.

Jensen, O. M.; Hansen, P. F. (1999): Influence of temperature on autogenous deformation and relative humidity change in hardening cement paste. *Cement and Concrete Research*, vol. 29, no. 4, pp. 567 – 575.

Jensen, O. M.; Hansen, P. F. (2001): Autogenous deformation and RH-change in perspective, *Cement and Concrete Research*, vol. 31, no. 12, pp. 1859 – 1865.

Kesavan, S. (1979): Homogenization of elliptic eigenvalue problems I. *Applied Mathematics and Optimization*, vol. 5 , no. 1, pp. 153-167.

Kesavan, S. (1979): Homogenization of elliptic eigenvalue problems II. *Applied Mathematics and Optimization*, vol. 5 , no. 1, pp. 197-216.

Lee, K. M.; Lee, H. K. (2006): Autogenous shrinkage of concrete containing granulated blast-furnace slag. *Cement and Concrete Research*, vol. 36, no. 7, pp. 1279–1285.

Li, Y. Y.; Cui, J. Z. (2005): The multi-scale computational method for the mechanics parameters of the materials with random distribution of multi-scale grains. *Composites Science and Technology*, vol. 65, no. 9, pp. 1447-1458.

Liu, S.; Liu X.; Guan, X. F.; He P. F.; Yuan, Y. (2013): A Stochastic Multi-scale Model for Predicting the Thermal Expansion Coefficient of Early-age Concrete. *CMES: Computer Modeling in Engineering and Science*, vol. 92, no. 2, pp. 173-191.

Liu, S.; Liu, X.; Yuan, Y.; He, P. F.; Mang, H. (2014): A Stochastic Multi-scale Model for Prediction of the Autogenous Shrinkage Deformations of Early-age Concrete. *CMC: Computers Materials and Continua*, 2014 (Accept).

Liu, X.; Liu, X. (2013): Full-Scale Test on the Early Age Performance of Im-

mersed Tunnel. Model Tunneling Technology, 2013 (Accept in Chinese)

Lura, P.; Breugel, K. V. (2001): Effect of curing temperature and type of cement on early-age shrinkage of high-performance concrete. *Cement and Concrete Research*, vol. 31, no. 12, pp. 1867 – 1872.

Lura, P.; Jensen, O. M. (2003): Autogenous shrinkage in high-performance cement paste: An evaluation of basic mechanisms. *Cement and Concrete Research*, vol. 33, no. 2, pp. 223–232.

Lura, P.; Jensen, O. M. (2009): Cracking in cement paste induced by autogenous shrinkage. *Materials and Structures*, vol. 42, pp. 1089 – 1099.

Maruyama, I.; Teramoto, A. (2011): Impact of time-dependant thermal expansion coefficient on the early-age volume changes in cement pastes. *Cement and Concrete Research*, vol. 41, no. 4, pp. 380– 391.

Mohamad, A. S.; Stéphane, L.; Loic, D. (2014): Coupling between mechanical and transfer properties and expansion due to DEF in a concrete of a nuclear power plant. *Nuclear Engineering and Design*, vol. 266, pp. 70– 77.

Nguyen, V. H.; Colina, H.; Torrenti, J. M. (2007): Chemo-mechanical coupling behavior of leached concrete Part I: Experimental results. *Nuclear Engineering and Design*, vol. 237, no. 20, pp. 2083–2089.

Nguyen, V. H.; Colina, H.; Torrenti, J. M. (2007): Chemo-mechanical coupling behaviour of leached concrete Part II: Modelling. *Nuclear Engineering and Design*, vol. 237, no. 20, pp. 2090–2097.

Paul, C.; Allan, C. L. (2007): Measurement of the coefficient of thermal expansion of ultra-high strength cementitious composites using fiber optic sensors. *Cement and Concrete Research*, vol. 37, no. 5, pp. 789 – 795.

Pichler, C.; Lackner, R.; Mang, H. (2007): A multi-scale micromechanics model for the autogenous-shrinkage deformation of early-age cement-based materials. *Engineering Fracture Mechanics*, vol. 74, no. 1, pp. 34–58.

Roman, L.; Beat, M.; Lura, P. (2010): A volumetric technique for measuring the coefficient of thermal expansion of hardening cement paste and mortar. *Cement and Concrete Research*, vol. 40, no. 7, pp. 1138–1147.

Ulm, F.; Coussy, O. (1995): Modelling of thermo-chemo-mechanical coupling of concrete at early ages. *Journal of Engineering Mechanics*, vol. 121, no. 7, pp. 785-793.

Ulm, F.; Coussy, O. (1998): Couplings in early-age concrete: from material modeling to structural design. *Journal of Solids Structures*, vol. 35, no. 31, pp. 4295-4311.

Wang, T. M. (1997): *Crack control of engineering structures*. Building Industry

Press, Beijing, China (In Chinese).

Wyrzykowski, M.; Lura, P. (2013): Controlling the coefficient of thermal expansion of cementitious materials – A new application for superabsorbent polymers. *Cement and Concrete Composites*, vol. 35, no. 1, pp. 49-58.

Ye, H. L.; Tian, Y. (2013): Influence of cracking on chloride diffusivity and moisture influential depth in concrete subjected to simulated environmental conditions. *Construction and Building Materials*, vol. 47, pp. 66–79.

Yeon, J. H.; Choi S. (2013): In situ measurement of coefficient of thermal expansion in hardening concrete and its effect on thermal stress development. *Construction and Building Materials*, vol. 38, pp. 306–315.

Yoo, S. W.; Kwon, S. J. (2012): Analysis technique for autogenous shrinkage in high performance concrete with mineral and chemical admixtures. *Construction and Building Materials*, vol. 34, pp. 1–10.

Zhang, J., Hou, D. W. (2010): Experimental study on the relationship between shrinkage and interior humidity of concrete at early age. *Magazine of Concrete Research*, vol. 62, no. 3, pp. 191–199.

Zhang, J.; Hou, D. W. (2012): Micromechanical modeling on autogenous and drying shrinkages of concrete. *Construction and Building Materials*, vol. 29, pp. 230–240.

Zhutovsky, S.; Kovler, K. (2004): Influence of cement paste matrix properties on the autogenous curing of high-performance concrete.   *Cement and Concrete Composites*, vol. 26, no. 5, pp. 499–507.